Journal of Colloid and Interface Science 727 (2027) 141646

Contents lists available at ScienceDirect

Journal of Colloid And Interface Science

journal homepage: www.elsevier.com/locate/jcis

DNA-decorated phase-shift microdroplets enable programmable coalescence and gene transfection

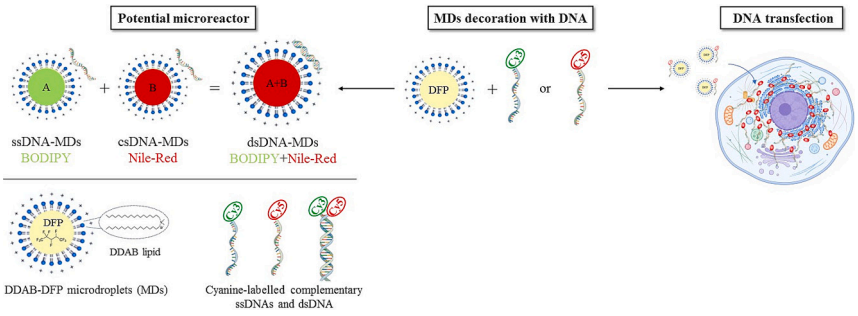
Giulia Perilli [1], Angela Ditri [1], Alessandra Vitaliti, Yosra Toumia, Alessandro Porchetta, Gaio Paradossi, Fabio Domenici [*]

Department of Chemical Science and Technologies, University of Rome "Tor Vergata", 00133 Rome, Italy

HIGHLIGHTS

- Versatile DNA-microdroplets assemblies are formulated and optimized.
- The complementary DNAs hybridization is exploited to induce selective coalescence.
- Microfluidic arrangements open the way in developing microreactors.
- The platform low cytotoxicity enables use at bio-interfaces.
- DDAB-MDs affinity for cell membrane is optimal for DNA-transfection in tumor cells.

GRAPHICAL ABSTRACT



ARTICLE INFO

Keywords:
Microdroplets
DDAB
DNA
Selective coalescence
Microreactors
DNA transfection
Gene therapy

ABSTRACT

Hypothesis: Phase-shift perfluorocarbon microdroplets (MDs) are a promising and flexible method for challenging applications in colloid science, such as customizing chemical reactions or enhancing tumor gene delivery efficiency. To achieve these goals, we focused on stable MDs made of a decafluoropentane (DFP) core and a dimethyldioctadecylammonium bromide (DDAB) lipid shell that binds DNA through electrostatic interactions to create DNA-MDs assemblies.

Experimental: The MDs were obtained via ultrasound homogenization and decorated with complementary DNAs. Fluorescence, confocal microscopy, and dynamic light scattering methodologies were combined to measure the binding features driving DNA-MDs formation and their coalescing interactions. The effect of the DNA-MDs at the cell interface was evaluated by MTT viability assay and DNA transfection in tumor melanoma cells.

Findings: We defined the colloidal formulation of DNA-MDs, functional for both chemical and biomedical relevant applications. First, we identified the conditions that enable DNA-MDs to rapidly and selectively coalesce via oligonucleotide hybridization at the MDs interface. Then, we used DNA-MDs to efficiently enter nucleic acids into human melanoma cells, even within a two-step transfection protocol to promote intracellular DNA strand displacement.

Our results could shed new light on conducting controlled reactions in small volumes, realizing microreactors, as well as designing consensus gene transfection strategies.

* Corresponding author.
E-mail address: fabio.domenici@uniroma2.it (F. Domenici).
[1] Equally contributing authors.

https://doi.org/10.1016/j.jcis.2026.141646
Received 7 June 2026; Received in revised form 5 September 2026; Accepted 19 September 2026
Available online 20 September 2026
0021-9797/© 2026 The Authors. Published by Elsevier Inc. This is an open access article under the CC BY-NC-ND license (http://creativecommons.org/licenses/by-nc-nd/4.0/).

1. Introduction

Perfluorocarbon (PFC) microdroplets (MDs) have emerged as a promising platform to address long-standing challenges in chemistry and enhance the efficiency of drug and gene delivery in nanomedicine [1–5]. Several notable advantages can be identified in this regard. In particular, MDs exhibit excellent stability and biocompatibility in the bloodstream, which enable prolonged visualization via multimodal imaging techniques [6,7]. Specifically, their liquid core makes them detectable by fluorine-19 magnetic resonance imaging [8,9] and solvatochromic markers embedded within make them visible by fluorescence methods [1]. As additional and relevant feature, the PFC core of the MDs can undergo liquid→gas phase transition triggered by ultrasound, optical, or ionizing radiation stimuli, which converts them into echogenic microbubbles (MBs) [1,4,10–12]. For this reason, PFC MDs are also called phase-change MDs and represent a class of ultrasound contrast agents of the vessel system. The so-generated MBs solicited by ultrasound have been demonstrated to increase drug permeation through tissue barriers, such as the blood-brain barrier (BBB) [5]. MDs core is often stabilized in water by a shell of variable composition, consisting of proteins, lipids, or biocompatible polymers, which can also be co-arranged to form hybrid double layers [6,13]. MDs coatings have been widely studied to facilitate active targeting and conjugation with therapeutic molecules, turning MDs into an invaluable theranostic platform against tumor-associated vasculature [14,15]. Although drug solubilization in the fluorinated core is often limited, this challenge can be mitigated through the inclusion of secondary oily phases or cosolvents such as ethanol [15].

While maintaining the shell stabilizing function, it is possible to design the surface to induce selective coalescence that leads to mixing of the cores contents. Moreover, the ausilium of microfluidic systems offering controlled high mixing rates can transform a process of high affinity surface interaction of two different MDs populations into reaction-controlled nano-reactors [16–18]. In other words, tailored coalescence between two microdroplets containing different reagents could be useful in developing microreactors, where the desired product of a specific reaction is obtained in a confined space only upon the mixing of microsphere content.

In general, the coalescence phenomenon is triggered by the collision of two drops of liquid touching each other for such a time as to induce a microscopic liquid bridge that grows rapidly until the two drops merge into one [19]. The volume of MDs formed by coalescence is equal to the sum of the starting droplets, while the total surface area is reduced, thus resulting in a more stable colloid. The mechanism of coalescing droplets dispersed in another continuous phase can be divided into three subprocesses depending on the distance between droplets (i.e., 1, the collision of two droplets trapping an interphase thin film of the continuous phase; 2, the drainage of the thin film due to the attraction between the droplets; 3, overcoming of the droplets surface tension leading to their fusion) [20–22]. This phenomenon is extensively studied but still not controllable since it is necessary to balance the MDs' relative velocity and the contact time between the drops to ensure that coalescence occurs rather than bouncing or fragmentation [19,23].

On this line, controlling the separation distance between the droplets' interfaces is crucial. The use of charged surfactants as components of the shell can make the coalescence phenomenon less likely due to repulsion, inducing a higher stability of the system for longer times [24]. In opposition to the repulsive forces of the shell, its decoration with high affinity binders can promote specific interaction between two MDs. In this mode the MDs can be kept in close contact for a sufficient time to destabilize their surface, resulting in a merger (i.e., in terms of coalescence sub-processes, this corresponds to increasing the probability that two distinct microdroplets coming into contact can complete the 2nd sub-process and trigger the 3rd one [22]). Designing MDs core-shell composition suitable for such multi-usage (i.e, tailoring the coalescence by MDs recognition, and gene delivery) would be of significant interest. In this respect, we have recently developed versatile and stable MDs made of dimethyldioctadecylammonium bromide (DDAB) shell and a liquid perfluorocarbon decafluoropentane (DFP) core. DDAB is a non-viral synthetic lipid vector with a positive charge on the quaternary ammonium, which attracts the negatively charged DNA backbone [25,26]. Some of us have previously reported the formulation for producing high density and narrowly polydispersed DDAB-MDs in water dispersion using a simple and rapid ultrasonic homogenization process [15]. This colloidal system exhibited high stability thanks to a high positive z-potential of the MDs shell [1] and the long-saturated DDAB chains embedded in the stable (b.p. 55 °C) partially fluorinated DFP core. Those physicochemical properties confer to the platform an invaluable potential as drug delivery carrier, especially in facilitating the transport of low hydrophilic drugs enclosed in the MDs core through polar biological environments and releasing them within tumor cells, limiting the side effects of treatments [1,15]. At the same time, the high affinity of DDAB MDs shell for cell membranes could be exploited to transfect nucleic acids in cells [25,27]. In this way, determined tumor pathways can be modulated through siRNAs and specific consensus sequences transfection, thereby inhibiting drug resistance [28,29]. Despite such a huge potential, the binding interaction of DNA strands onto the MDs DDAB shell at the aqueous interface remains, to date, unveiled.

Here, we not only provide novel insights into these interactions, but also exploited them to control droplet coalescence. Specifically, we hypothesized that an appropriate MDs to DNA ratio could promote selective fusion between differently loaded MDs populations via strand hybridization. At the same time, the DNA-decorated surface should maintain a sufficiently high ζ-potential to prevent nonspecific aggregation, according to DLVO and heterogeneous surface charge interaction theories [30–33].

Motivated by the above arguments, in the first part of the study we take advantage of the intrinsic programmability of Watson-Creek-Franklin interactions to induce rapid and selective MDs coalescence controlled by hybridization and strand displacement reactions between complementary DNA strands [34–36]. This application represents a recent development in the field of microfluidics; to our knowledge, there are no explanatory studies in the literature exploring it yet. Optimizing this process is particularly appealing for chemical information transfer and microreactors development.

In the second part of the work, we report on tumor cells transfection mediated by the affinity of DDAB-shelled MDs for the cell membrane. Using DNA-decorated MDs we demonstrate that nucleic acids can be conveyed and introduced into the cell, paving the way for their use as vectors for the transfection of consensus genes in non-viral gene therapy.

For the first purpose, two different populations of MDs were prepared, each loaded with an organic molecule and covered with a complementary single strand of DNA (ssDNA and csDNA). As a proof-of-concept study, we opted for two fluorophores, Nile Red and BODIPY FL, as model molecules to be encapsulated in the MDs core, in order to prove the mixing of the two populations contents driven by ssDNA hybridization. This evidence turns the MDs into novel colloidal compartments in which species or reactions can be isolated and controlled at the micrometer scale. Moreover, such a platform appears ideal for quantitative studies and enables the manipulation of extremely small volumes, which is particularly useful for high-throughput experiments. Microfluidics may be the most appropriate survey methodology for this system as it can monitor the collision and coalescence of droplet populations.

The second challenge is delivering DNA into cells. In the present work, we use DNA-MDs also as a non-viral DNA transfection into a skin melanoma cell model (SK-MEL-28). In order to induce and control the coalescence process between droplets as well as to follow the DNA transfection, we use fluorescence-labeled short sequences of ssDNA. In particular, we took advantage of the FRET phenomenon given by Cyanine3 (Cy3) and Cyanine5 (Cy5) fluorophores, which were linked to the complementary nucleic acids to monitor their hybridization. Moreover, the process was also investigated in the presence of an invading

strand (isDNA): when an isDNA reversibly dissociates a preformed double strand (dsDNA), giving a new helix and a new outgoing ssDNA, a displacement reaction occurs [37,38]. In molecular biology, this process is regulated by enzymes such as polymerases [39]. In the absence of enzymes, the hypothesized reaction mechanism occurs in two stages [40,41]: the dsDNA is attacked by the isDNA to give first an intermediate product, followed by the detachment of a ssDNA and the formation of the new helix. The second stage is the kinetically determinant one. The displacement reaction occurs mainly because the isDNA has a toehold that allows it to hybridize fully. The process rate is influenced, among other factors, by the toehold length: the greater the number of nucleotides in the toehold, the faster the reaction and the less invader is needed for the reaction to take place.

Herein, combined photocorrelation, spectrofluorimetry, and time-lapse confocal laser scanning microscopy (CLSM) analyses allowed the development of an optimized DNA-MDs formulation exhibiting high affinity of DNA hybridization, capable of triggering selective coalescing interaction, and even facilitating intracellular DNA displacement.

2. Materials and methods

2.1. Materials

Dimethyldioctadecylammonium bromide (DDAB, ≥98%; TLC), 1,1,1,2,3,4,4,5,5,5-decafluoropentane (DFP, purity 60%; GC), 9-diethylamino-5-benzo[*a*]phenoxazinone (Nile Red, ≥98%; HPLC), ethanol (puriss. p.a., absolute, ≥99.8%; GC) were purchased from Sigma-Aldrich (St. Louis, MO, USA). Sterile phosphate-buffered saline solution (PBS, 0.15 M, pH = 7.4) was purchased from Corning (Corning, NY, USA). Milli-Q water (resistivity 18.2 MΩ•cm) was produced using a Millipore (Burlington, MA, USA) water purification system with a 0.22 μm final filter. BODIPY FL L-Cystine was purchased from Probes by Life Technologies (Carlsbad, CA, USA). Lyophilized DNA samples (DNA-Cy5, 5′-modified with Cy5: CY5-CGT GAC CTA TGC CAT TCT ATT TGA; DNA-Cy3, 3′-modified with Cy3: AGA ATG GCA TAG GTC ACG-CY3; isDNA, unmodified: TCA AAT AGA ATG GCA TAG GTC ACG) were provided by IBA Solutions for Life Sciences (Goettingen, Germany) and HPLC purified. For cell cultures and assays, human melanoma SK-MEL-28 cell line was provided by Interlab Cell Line Collection (ICLC, National Cancer Research Institute, GE, IT), and cultured in DMEM without phenol red (Corning, Corning, NY, USA) with 1% Pen/Strepto (Sigma-Aldrich, St. Louis, MO, USA), 1% L-Glutammine and 10% FBS (Fetal Bovine Serum; Corning, Corning, NY, USA). 3-(4,5-Dimethylthiazol-2-yl)-2,5-diphenyltetrazolium bromide (MTT, 98%) and Calcein-AM solution (4 mM in DMSO, ≥ 90%; HPLC) were purchased from Sigma Aldrich (St. Louis, MO, USA). Hoechst 33342 (trihydrochloride, tryhydrate) solution (16.2 mM in water; ≥ 98%) was obtained by Invitrogen by ThermoFisher Scientific (Waltham, MA, USA).

2.2. Bare MDs preparation and characterization

Undecorated MDs with a DFP core and a DDAB shell (see SM, section S1.1, Fig. S1), dispersed in PBS, were prepared following the steps described in [15]. Specifically, 250 μl of DFP, 300 μl of DDAB solution (6 mg/ml in EtOH), and 2.15 ml of PBS (diluted from stock solution to 0.01 M, pH = 7.4) were added in this order in a 15 ml falcon tube. PBS dilution was chosen in order to prevent colloidal instability related to salt effects. The mixture was sonicated with an ultrasonic set-up vibracell VCX-400 equipped with a 1/8″ (3 mm) in titanium tapered microtip (Sonics&Materials, Newtown, CT, USA) for 10 s (0.7 s pulse on +0.3 s pulse off, 20 kHz, 400 W, 35% amplitude) and quickly diluted adding PBS by a factor of 1.8. The dilution factor is indicative and empirically chosen according to the colloidal stability and concentration required for the specific application. By following this procedure, the simultaneous production of DDAB vesicles with an aqueous core (e.g. SUVs, LUVs) is avoided, as the DDAB Krafft temperature [1] is not reached in the working conditions. Consequently, the gel-liquid phase transition of the lipid chains, necessary to obtain such structures, is prevented, as confirmed by CLSM analyses (see SM, section S1.1, Fig. S2 a-c), and DDAB is expected to form a layer at the DFP-water interface. In order to obtain MDs containing fluorescent dyes in the core, 20 μl of the chosen fluorophore solution (Nile Red or BODIPY, 10 μg/ml in EtOH) was added in the DFP phase of the mixture just before the sonication. In both cases, the characterization of the system morphology was carried out by CLSM using a Nikon Eclipse Ti-E inverted confocal microscope (Nikon, Tokyo, Japan), equipped with an Argon ion laser (Spectra Physics, Mountain View, California; emission wavelength 488 nm) and He—Ne laser (Melles Griot, Carlsbad, California, USA; emission wavelength 543 nm), either in transmission or laser scanning mode. Images were acquired with 40× (air) or 60× (oil immersion) objectives using EZ-C1 software, version 3.91 (Nikon, Tokyo, Japan). According to this procedure, a number density of $\sim 9{\cdot}10^9$ MDs/ml was obtained, as determined by microscopy using a Neubauer counting chamber (BRAND GMBH, Wertheim, Germany). In the area of interest, four images were recorded using a 40× objective and then analyzed by the ImageJ open-source program (NIH Image, Bethesda, MD, USA). In order to also detect droplets with diameter < 1 μm, the MDs counting was further verified manually on a slide, by acquiring several images using a 60× objective. The final concentrations were expressed as MDs/ml and calculated with the following eq. (1):

$$\frac{MDs}{ml} = \frac{number\ of\ droplets \bullet 1000 \times (diluition\ factor)}{(0,0625\ mm^2) \bullet (0,1\ mm)} \quad (1)$$

The mean hydrodynamic diameter and size distribution of MDs were measured by Dynamic Light Scattering (DLS) at 25 °C using a Hamamatsu HC120 photometer (Brookhaven Instruments, NY, USA), equipped with a BI-200SM goniometer set at 90° with a BI-9000 AT photocorrelator and solid-state laser (Suwtech. Inc., Shangai, China, wavelength 532 nm). Each measurement was acquired for 2 min, performed in triplicate on distinct sample batches and repeated for each sample on subsequent days to assess colloidal stability [1]. The hydrodynamic diameter values were further confirmed by Non-Invasive Back Scatter DLS (NIBS) detection at 173° using a Zetasizer Nano particle analyzer (MalvernPanalytical, Malvern, UK), corroborating the absence in the dispersion of nanometric vesicles in the dispersion as well as DDAB thin films at the air-water interface (see SM, section S1.1, Fig. S2 d-f). Furthermore, MDs Zeta potential in PBS was determined by DLS (Zetasizer Nano, MalvernPanalytical, Malvern, UK) to evaluate the system stability in saline buffer (see SM, section S1.1, Fig. S3). The measurement was carried out using a disposable closed capillary electrophoresis cell (DTS1070-Malvern Panalytical, Malvern, UK), made of polycarbonate with integrated gold-plated copper electrodes.

2.3. DNA-coated MDs preparation and characterization

For this study, DNA-decorated MDs were prepared by selecting an appropriate DNA-to-MDs ratio, optimized according to the system colloidal stability as well as to set the fluorescence from the cyanine fluoroprobes linked to DNAs in a proper dynamic range for detection (i.e., avoiding either poor or saturated signals). All DNA samples were resuspended in PBS (0.01 M, pH 7.4), divided into 100 μM aliquots, and stored at −20 °C. Before each measurement, the DNA aliquot was thawed and diluted in PBS to a concentration of ~10 μM. Tecan's NanoQuant Plate (Tecan Group Ltd., Salzburg, Austria) was used for the quantification of small volumes (2 μl) of nucleic acids in absorbance mode using the $A_{260\ nm}$ value in Lambert-Beer's law and for the measurement of the labelling efficiency of ssDNAs conjugated with fluorescent dyes. The preparation was carried out as follows: 10 nM of ssDNA was added to 1×10^6 MDs/ml suspension in PBS at a volumetric ratio 1:1. An MDs concentration far below the $\sim 9 \times 10^9$ MDs/ml value was chosen to prevent short-term coalescence. Then, at the fixed number density of 1×10^6 MDs/ml, the colloidal stability of the system was

evaluated at different Cy-ssDNA concentrations, to define the suitable amount of DNA (see SM, section S1.2, Fig. S4). To verify if any variations occur to the cyanine's emission in the DNA-MDs samples, fluorescence spectra of the different conditions (free or bound-DNA) were acquired (see SM, section S1.2, Fig. S5a). Further, Cy3 emission spectrum was acquired in the Cy3-ssDNA-MDs supernatant, collected after sample centrifugation for 3 min at 1480 rpm and RT, in order to detect any signal deriving from free labeled-DNA in solution. No significant emission was observed (see SM, section S1.2, Fig. S5b); thus, the purification step was not introduced in the formulation protocol avoiding useless sample manipulation. DNA-MDs morphology, size distribution and Zeta potential (see SM, section S1.2, Fig. S6) were analyzed in the same way described for undecorated MDs, thus by using CLSM and DLS. Specifically, the CLSM analyses were carried out following the green and red fluorescence emission of Cy3 and Cy5 bound to the DNAs. The coated surface degree at the working conditions, α', was calculated from the fluorescence analysis of a 10 nM solution of ssDNA-Cy3 to which increasing additions of bare MDs were made (see SM, section S1.3, Fig. S7). Hence, a geometrical calculation based on steric hindrance of DNA onto the MDs was performed, leading to an estimate of the number of DNA molecules decorating a MD (see SM, section S1.3., Fig. S8).

2.4. DNA hybridization kinetics

The ssDNA hybridization kinetics was studied in PBS solution (0.01 M, pH = 7.4), at room temperature, through fluorescence measurements with a Spark multimode microplate reader (Tecan Group Ltd., Salzburg, Austria) in a 96-well black Polystyrene Microplate (Corning, Corning, NY, USA) in two different conditions: on free cyanine-labeled-ssDNAs in PBS and on a system with ssDNA-Cy3-MDs + free csDNA-Cy5. The hybridization of the two complementary DNAs induces a strong proximity of the two cyanines, which act as donor (Cy3) and acceptor (Cy5) in a FRET event. So, the kinetics was analyzed exciting at the Cy3 absorption wavelength (λ_{exc} = 525 nm) and following the increase of the Cy5 emission signal (λ_{em} = 675 nm) for 1 and a half hours. The general parameters set on the instrument were: interval time = 10 s, mode = top reading, band $width_{exc/em}$ = 20 nm, number of flashes = 30, gain = 140, *Z*-position = 17,000 μm, integration time = 40 μs. For the free ssDNAs measurements 100 μl of ssDNA-Cy3 (10 nM in PBS) and 100 μl of ssDNA-Cy5 (10 nM in PBS) were added to a well. The experiments were performed in triplicate and compared to a control (PBS). The collected data were analyzed using Origin Pro 8 software (OriginLab Corporation, Northampton, MA, USA) and fitted according to a monoexponential equation, from which the apparent direct kinetic constant (k_1) value was determined. To confirm the adequacy of the selected model, the data were also fitted with the corresponding linear equation. For ssDNA-MDs, the hybridization kinetics were followed on a pre-formed system obtained by adding 20 nM ssDNA-Cy3 to 2 × 10^6 MDs/ml (1:1), to which 10 nM of csDNA-Cy5 was added in a volumetric ratio 1:1. Furthermore, the ssDNAs adsorption kinetics on MDs surface was followed as a control experiment (see section S1.4., Fig. S9). In both latter cases, instead of the FRET signal, the donor emission was followed (λ_{exc} = 525 nm, λ_{em} = 570 nm, see SM, section S1.5, Fig. S10), and the measured sample was compared to MDs in PBS as control. All other instrument parameters were left the same as seen above, and the measured data were fitted with the previously cited equation expressed in terms of ssDNA-Cy3 emission.

2.5. DNA binding affinity

The complementary DNAs hybridization was followed at a fixed concentration of ssDNA by adding increasing amounts of csDNA, to determine the binding affinity of the ssDNAs. Even in this case, the experiments were carried out, at room temperature, on free cyanine-labeled-ssDNAs in PBS (0.01 M, pH = 7.4) and on a system with ssDNA-Cy3-MDs + free csDNA-Cy5. A wide range of csDNA-Cy5 was studied (1–300 nM): the donor emission spectra (530 nm < λ < 645 nm) were acquired for each condition and for the ssDNA-Cy3 alone on a Spark fluorimeter in a 96-well black polystyrene microplate. If not specified elsewhere, the general parameters set on the instrument are to be considered the ones cited in paragraph 2.4. For the measurements on free ssDNAs, the fixed concentration of ssDNA-Cy3 used was 10 nM, while for the ssDNA-Cy3-MDs experiments, the system was composed of 20 nM ssDNA-Cy3 + 2 × 10^6 MDs/ml (1:1). For both cases, the value of the fluorescence maximum of every spectrum was then used to build a hyperbolic curve, where the y-axis was obtained by difference between the maximum value of donor emission alone in PBS and the same value at the different csDNA-Cy5 concentrations examined (expressed as Δ_{RFU}). These data have then been plotted against the [csDNA-Cy5] and the graph was fitted as follows to determine the equilibrium dissociation constant (K_{obs}), which is related to the binding affinity. In order to obtain a more reliable value for K_{obs}, the fit has then been iterated till convergence for both cases. For free ssDNAs the following classical Langmuir binding isotherm eq. (2), which assumes a reversible interaction between complementary DNA strands with a 1:1 stoichiometry and independent binding sites, was used [42,43]:

$$\Delta_{RFU} = \frac{RFU_{\infty} \bullet [ssDNA - Cy5]}{K_{obs} + [ssDNA - Cy5]}, \quad (2)$$

where [ssDNA-Cy5] represents the concentration of free ssDNA-Cy5 and RFU_{∞} and K_{obs} are fit parameters corresponding respectively to the curve plateau value and the equilibrium dissociation constant. Instead, for the ssDNA-MDs system, eq. (3) was applied:

$$\Delta_{RFU} = \frac{RFU_{\infty} \bullet [ssDNA - Cy5]}{K_{obs} + [ssDNA - Cy5]} + C \bullet [ssDNA - Cy5] \quad (3)$$

where the variables are the same as described in eq. (2) and C represents a supplementary fitting parameter, corresponding to the slope of the additional linear contribution to Langmuir eq. (2). This equation is an empirical expression derived from the classical Langmuir binding isotherm (Eq. 2) taking into account not only the complementary DNA hybridization equilibrium, but also the competitive adsorption of ssDNA-Cy5 onto the MDs surface. Further information about the derivation, physical meaning and statistical analysis of eq. (3) is given in SM, section S1.6, Figs. S11 and S12 and Table S1.

2.6. Strand displacement reaction

The strand displacement reaction has been studied, at room temperature, with a Spark fluorimeter (Tecan Group Ltd., Salzburg, Austria) on free dsDNA + free isDNA in PBS (0.01 M, pH = 7.4) and on a system with dsDNA-MDs + free isDNA. The reaction was performed at a fixed concentration of a pre-hybridized dsDNA (ssDNA-Cy3 + csDNA-Cy5, 10 nM) by adding increasing amounts of a non-modified isDNA, complementary to ssDNA-Cy5 and with a toehold made up of six nucleotides (6-nt) (200, 300, 400 nM). When the displacement reaction occurs the two cyanines are brought far from each other, leading to a decrease of the FRET signal. The reaction was monitored 15 min after the mixing of the reactants for each [isDNA] tested, either by the acquisition of the donor emission spectra (480 nm < λ < 580 nm), or by following the FRET signal for 22 min. The experiments were performed in triplicate and compared to PBS solution and dsDNA 30 nM without isDNA as control samples. For the dsDNA-MDs (pre-formed 20 nm dsDNA +2 × 10^6 MDs/ml, 1:1) + free isDNA system, also higher concentrations of isDNA were tested, up to 3 μM.

2.7. Spectrofluorometric data analysis

If not specified otherwise, the fluorescence spectra were analyzed as follows: a five-point Savitzky-Golay smoothing was applied to the raw data, and a four-point baseline was drawn for each curve and subtracted using the Origin Pro 8 software (OriginLab Corporation, Northampton, MA, USA).

2.8. ssDNA-MDs interaction

The study of the complementary ssDNA-MDs interaction was performed using DLS measurements (Hamamatsu HC120 photometer; Brookhaven Instruments, NY, USA, see paragraph 2.2) to verify the presence of any coalescence phenomena. For this analysis, the ssDNAs had the same sequences used so far, but were unlabeled. Two MDs populations were prepared in PBS (0.01 M, pH = 7.4) maintaining the optimized working conditions (10 nM ssDNA $+1 \times 10^6$ MDs/ml; A = ssDNA-MDs; B = csDNA-MDs). Each sample was first analyzed alone, at room temperature, and its size distribution was determined; then coalescence events were followed by adding A to B in a 1:1 ratio. The measurements were made from the mixing time and followed for a total of 5 h with acquisition every 30 min. Non-specific coalescence (A + A) was further tested in a control sample, specifically selected to exclude the possibility of MDs fusion induced by non-complementary strands interactions. Coalescence events were also studied via CLSM on ssDNA-MDs containing fluorophores, to simulate the encapsulation of reagents and better characterize the process time scale. In this case, the two populations were labeled with BODIPY, i.e. ssDNA-BODIPY-FL-MDs (A) and Nile Red, i.e. csDNA-Nile-Red-MDs (B), respectively; if localized in the same drop, these dyes act as donor (BODIPY) and acceptor (Nile Red), giving a FRET signal [44]. A and B populations were brought together in an IBIDI μ-Slide 4 well (final volume = 300 μl; IBIDI, Martinsried, Germany) and time-lapse videos were acquired to follow the coalescence events in real time. Red and green fluorescence channels were acquired separately using specific excitation and emission CLSM settings, suitably chosen to minimize spectral overlap of the two fluorophores and direct excitation of Nile-Red during BODIPY acquisitions. The parameters set on CLSM were λ_{exc} = 488 nm, λ_{em} = 515–530 nm, pinhole = large, gain = 7.30 for green laser and λ_{exc} = 543 nm, λ_{em} = 650 nm, pinhole = medium, gain = 7.10 for red laser. For both, pixel dwell = 1.92 μs and the time between two consecutive frames was set to = 1.240 s. Using ImageJ Fiji software, microscopy-based size analyses were performed on individual droplets on the first and last frames of coalescence time-lapse videos to build the corresponding size distributions. The relative histograms were plotted and fitted with a Gaussian equation using Origin Pro 8 software to obtain the MDs mean diameter at t_0 (before A + B mixing) and at t_f (at the end of the coalescence video). Mean fluorescence intensity analyses were performed on different frames of the CLSM time-lapse videos using ImageJ Fiji software, to build the corresponding curves for red and green channels. The intensities were measured on constant fields of view (ROIs of constant areas) to reduce possible optical effects associated with MDs size changes after coalescence. Being the quantum yields and the CLSM gains different for BODIPY and Nile-Red dyes, the obtained data for both signals were normalized with respect to their maximum value for appropriate comparison.

Finally, the enhancement of coalescence events was evaluated using a microfluidic arrangement. Separate 100 μl aliquots of each MD population were injected into an IBIDI μ-Slide III ^{3in1} channel (IBIDI, Martinsried, Germany) using two syringes connected to a pump. The flow properties were systematically optimized based on preliminary DLS sizing of the collected outlets to ensure both process reproducibility and effective droplet contact. The definitive steady-state conditions were established at an injection rate of 0.89 ml/min, corresponding to a shear stress of 5 dyn/cm^2. The fluid flow was monitored at room temperature via CLSM (Nikon Eclipse Ti-E), and time-lapse videos were acquired in transmission mode. For the subsequent analysis, a single representative video was selected for each of the two pivotal experiments (A + A and A + B). Droplet trajectories within the mixing region proximal to the channel junction – where fluid mixing induced variable velocities and interaction events - were tracked and quantified using NIS-Elements AR Analysis software (version 4.30.02, 64-bit, Nikon Corporation, Tokyo, Japan). Individual particles were identified by applying a size threshold (1–6 μm) to define the objects of interest and exclude artifacts or debris. For each recognized MD, a unique tracking label was assigned, and the corresponding trajectory was resolved by mapping its coordinates in space (along the XY plane) and time. From these discrete spatio-temporal coordinates, the software calculated the instantaneous kinematic and geometric parameters at each frame. Specifically, the particle speed (calculated as the resultant velocity along the XY plane, μm/s), acceleration (μm/s^2), surface area (μm^2), and equivalent diameter (μm) were extracted. The equivalent diameter was calibrated from pixel dimensions to match the physical sizes determined via static imaging. In total, the reported values represent the elaboration of more than 90 individual trajectories for the A + A control and over 400 trajectories for the interactive A + B system, comprehensively capturing baseline flow profiles and selective coalescence events. Detailed computational workflows, velocity distributions, and representative frames are provided in section S1.7 and Figs. S13 and S14 of the SM. Furthermore, the reaction product was collected for subsequent DLS size analysis.

2.9. MTT assay

The cytotoxicity of the MDs, ssDNAs and ssDNA-MDs against SK-MEL-28 cell line (human melanoma) was assessed by the MTT viability assay, which determines cellular metabolic activity. The cells were seeded in a 96-well flat plate at a density of 15,000 cells/well and treated after 24 h with MDs or ssDNAs alone and in combination. For what concerns MDs alone, different concentrations have been tested, ranging from 3.3×10^6 to 1.6×10^8 MDs/ml. The unlabeled-ssDNAs effect on the cells was determined between 0.05 and 2.8 nM. For biological applications of DNA-MDs systems, a DNA-strands/MDs ratio of 10^4 was defined and, according to that, four different concentrations have been tested: 0.05 nM ssDNA $+3.3 \times 10^6$ MDs/ml, 0.28 nM ssDNA $+1.6 \times 10^7$ MDs/ml, 0.55 nM ssDNA $+3.3 \times 10^7$ MDs/ml and 2.8 nM ssDNA $+1.6 \times 10^8$ MDs/ml. After 24 h the cells were washed with PBS (0.15 M, pH = 7.4) and then incubated for 3 h with MTT solution at a final concentration of 0.5 mg/ml in cell culture medium, at 37 °C under 5% CO_2. Then, MTT was removed and the formed purple formazan crystals were dissolved using 200 μl of DMSO/well. The solution absorbance was measured with a Spark multimode microplate reader (Tecan Group Ltd., Salzburg, Austria) at the formazan absorbance maximum wavelength (λ_{max} = 554 nm) and at a reference wavelength (λ_{ref} = 690 nm). For the blank, the MTT solution was incubated for 3 h in a well with no cells; after its removal 200 μl of DMSO were added. The absorbance of the blank and the control sample, made of untreated cells, at λ_{max} and λ_{ref}, was also acquired. Each condition was measured five times. From the absorbance values, the cell viability was calculated using the following eq. (4):

$$\text{Viability } (\%) = \frac{\overline{\text{Abs}_{\text{treated}}} - \overline{\text{Abs}_{\text{blank}}}}{\overline{\text{Abs}_{\text{ctrl}}} - \overline{\text{Abs}_{\text{blank}}}} \text{ x } 100, \quad (4)$$

where $\overline{Abs_{treated}}$ represents the mean of the absorbance values of the treated cells, $\overline{Abs_{blank}}$ is the mean absorbance of the blank and $\overline{Abs_{ctrl}}$ stands for the mean absorbance of the untreated cells. The viability values were plotted in a histogram against the treatment concentration for each condition.

2.10. Tumor cell DNA – Transfection

The feasibility of using DNA-MDs as transfection vector in human

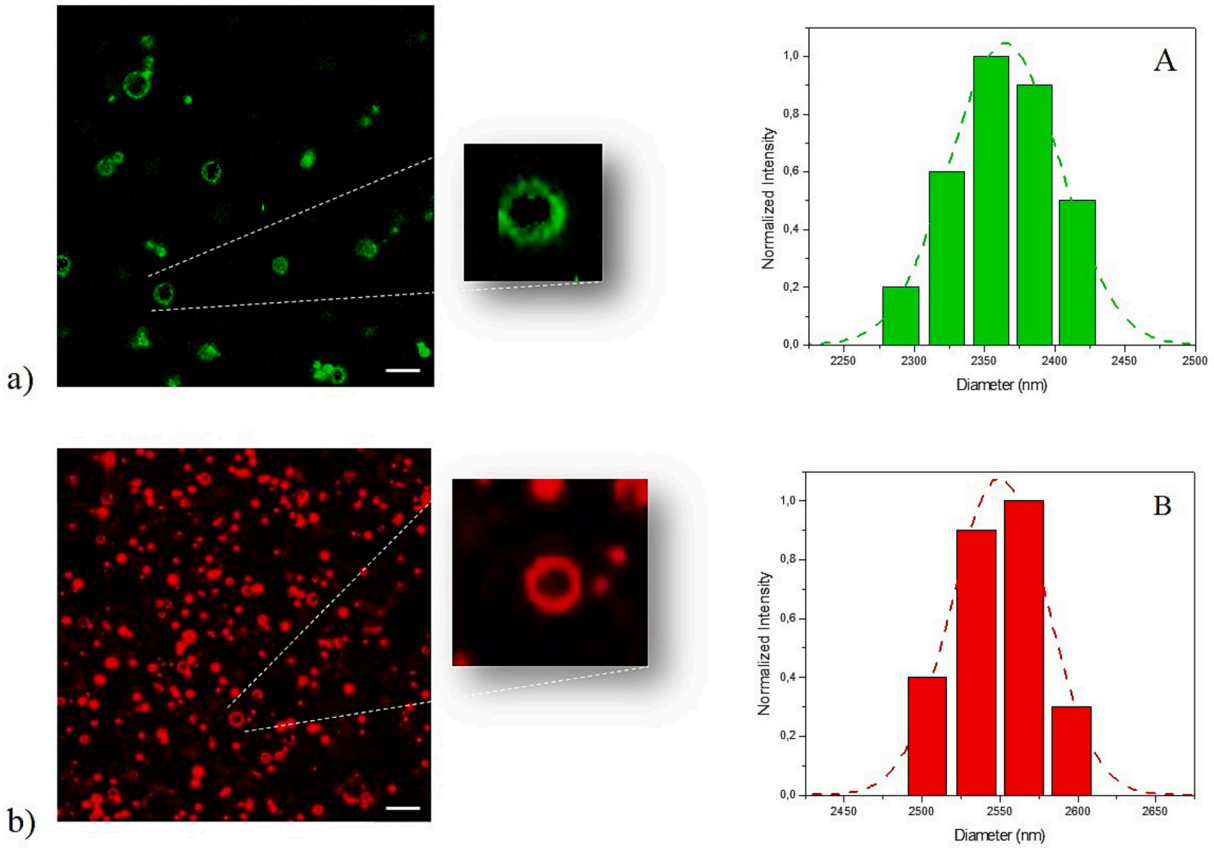


Fig. 1. Confocal fluorescence image of MDs covered by ssDNAs (left) and corresponding size distribution obtained by DLS measurements (right): a) population A (ssDNA-Cy3-MDs), average diameter ± σ = 2.36 ± 0.03 μm b) population B (csDNA-Cy5-MDs), average diameter ± σ = 2.55 ± 0.04 μm a-b) objective 60×, scale bar 20 μm.

cells was evaluated on SK-MEL-28 cell line via CLSM experiments. For these studies a DNA-strands/MDs ratio of 10^4 was defined. The cells were seeded in 75 cm^2 flasks and maintained in a cell culture incubator at 37 °C, 5% CO_2. For the experiment, the cells were seeded in a μ-Slide 8 well^{high} (IBIDI, Martinsried, Germany) at a density of 20,000 cells/well and left overnight. Then, the culture medium was discarded and 300 μl of DNA-MDs (11 nM ss or dsDNA +6.6 × 10^8 MDs/ml, 1:1) were added to the cells, after dilution 1:10 in fresh culture medium in order to reach the desired final concentration (0.55 nM ss or dsDNAon 3.3 × 10^7 MDs/ml). The system was incubated at 37 °C, 5% CO_2, for two hours and then washed several times with PBS (0.15 M, pH = 7.4) to remove the MDs and any free DNA outside the cells. Next, cell culture medium was substituted with DMEM incorporating Hoechst 33342 (16.2 mM; dilution 1:5000) and Calcein-AM (4 mM; dilution 1:1000), to stain the cells nuclei and cytoplasm. Finally, the cells were observed under a CLSM microscope (Nikon Eclipse Ti-E), to verify if the DNA has been transfected. *Z*-stack images of Hoechst 33342 and Calcein-AM-stained cells were acquired using a Nikon-Eclipse Ti2-E inverted confocal microscope (Nikon, Tokyo, Japan); equipped with a semiconductor laser (Coherent Inc., Santa Clara, CA, USA; emission wavelength 405 nm), an Argon ion laser (Spectra Physics, Mountain View, California; emission wavelength 488 nm) and diode-pumped solid-state (DPSS) laser (Melles Griot, Florence, Italy; emission wavelength 561 nm) in laser scanning mode. Images were acquired with a 60× oil immersion objective and reconstructed using Nis-Elements AR software, version 5.01.00, 64 bit (Nikon Corporation, Tokyo, Japan). A second treatment was performed by removing the medium, adding isDNA-MDs 300 nM in fresh culture medium, incubating for 45 min and rinsing several times with PBS (0.15 M, pH = 7.4) before acquiring CLSM images. The system was imaged both in transmission and in laser scanning mode using a 60× objective.

3. Results and discussion

3.1. DNA-coated MDs characterization

For this study, MDs made of DFP core and DDAB shell were decorated with ssDNA-Cy3 (population A) or ssDNA-Cy5 (population B), defining the synthesis conditions and a ssDNA to MDs concentration ratio, according to Sections 2.2 and 2.3 (see also SM, sections S1.1 and S1.2). The morphology, size distribution and Zeta potential of ssDNA-MDs were pointed out via CLSM and DLS. The confocal images of the two different populations of MDs and the corresponding mean diameter distributions are reported in Fig. 1.

As shown in the CLSM micrographs, the ssDNAs are localized onto the DDAB-shelled MDs, displaying a characteristic ring-like structure or well-defined fluorescent spots depending on the droplet size and confocal plane sectioning. This localization makes the system fluorescent in green (Cy3) or red (Cy5), according to the population. In fact, MDs spontaneously capture the DNA via electrostatic interaction between the positively charged DDAB quaternary ammonium groups and the anionic DNA phosphate backbone. The positioning of the DNA on the MD surface influences cyanine's emission spectra, leading to a decrease in fluorophore intensity and a shift of the emission maximum to higher wavelengths (see SM, section S1.2, Fig. S5a), although remaining well detectable also by CLSM. This result aligns with previous reports and is caused by changes in the fluorophore's chemical environment in the buried conformation, which strongly affects the excited state [45]. Regarding the MDs dimensions, ssDNA-decorated MDs are larger than bare MDs, which have a distribution centered at 1.4 ± 0.1 μm (see SM, section S1.1, Figs. S1 and S2), with mean diameters of approximately 2.36 ± 0.03 μm for population A and 2.55 ± 0.04 μm for population B

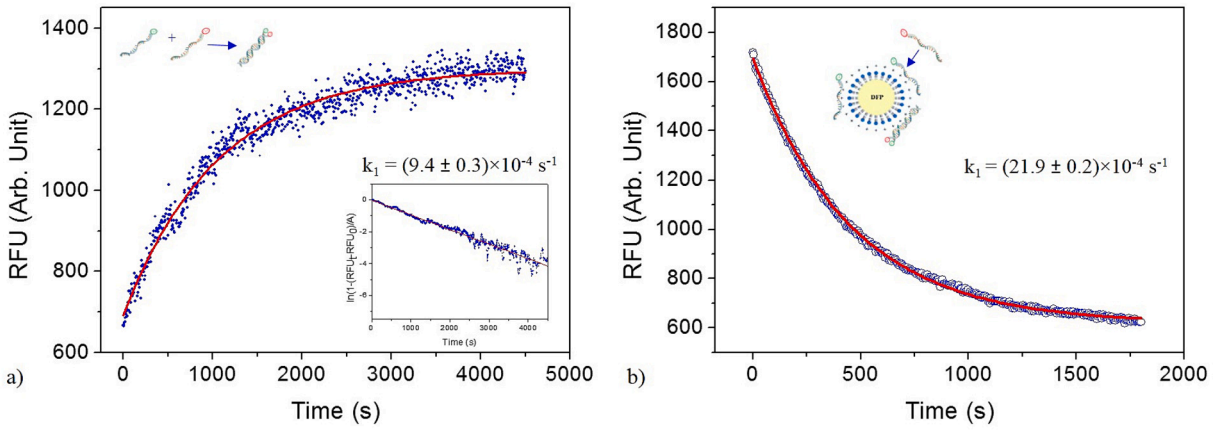


Fig. 2. ssDNAs hybridization reaction kinetics: a) FRET signal of a 10 nM ssDNA-Cy3 + 10 nM csDNA-Cy5 (1:1) solution. The curve fit (red) follows a monoexponetial equation, apparent $k_1 = (9.4 \pm 0.3) \times 10^{-4}$ s^{-1}, $R^2 = 0.97$. In the insert: FRET signal linearized according to the corresponding first order integrated kinetic equation together with the best fit (red) b) donor emission at $\lambda_{em} = 570$ nm of a 10 nM ssDNA-Cy3 on 10^6 MDs/ml + 10 nM csDNA-Cy5 (1:1) dispersion. The curve fit (red) follows a monoexponetial equation, apparent $k_1 = (21.9 \pm 0.2) \times 10^{-4}$ s^{-1}, $R^2 = 0.99$. All the experiments were performed in PBS according to section 2.4. (For interpretation of the references to colour in this figure legend, the reader is referred to the web version of this article.)

(Fig. 1a-b, right panels), as determined by Gaussian fit of the DLS curve analysis. This MDs size increase likely arises from rearrangement caused by the ssDNA decoration. The effects of DNA decoration on colloidal stability were also studied via Zeta potential measurements, yielding a characteristic $\zeta \sim +24$ mV for DNA-MDs, indicating a reduction in surface potential but still within a stability regime, compared to the bare system, which showed $\zeta \sim +78$ mV (see SM, section S1.1, Fig. S3 and section S1.2, Fig. S6). The measured positive ζ-potential for DNA-decorated MDs avoids complete charge neutralization and destabilization of the surface, thus preventing undesirable coalescence and/or aggregation phenomena.

3.2. ssDNAs hybridization kinetics on MDs surface

In order to characterize the interaction between the two complementary DNA strands, the ssDNA hybridization kinetics in solution was studied under two different conditions: on free ssDNAs in PBS and on a system with ssDNA-Cy3-MDs + free csDNA-Cy5. The cyanine DNA labelling allowed the ssDNA hybridization to be followed either by the increase of the Cy5 signal, due to a FRET phenomenon in which Cy3 acts as donor and Cy5 as acceptor, or by the decrease of Cy3 emission. The experimental curve of the free DNAs kinetic is reported in Fig. 2a: in this case the acceptor signal has been monitored and the trend shows an increase in its emission intensity, confirming the two strands proximity and the occurrence of FRET. Although DNA hybridization is intrinsically a bimolecular process, the acquired data have been fitted with a monoexponential equation (red curve), from which the apparent kinetic constant of the direct reaction has been obtained, resulting in $k_1 = (9.4 \pm 0.3) \times 10^{-4}$ s^{-1}. This fitting model procedure was selected assuming DNA hybridization as a multistep process where the observed fluorescence reflects the relaxation of the rate-determining step. Over at least three times the reaction half-life, this relaxation yields an apparent first-order kinetic constant rather than the intrinsic bimolecular one. This behavior aligns with literature on DNA hybridization and conformational transitions, where the emergence of first-order kinetics is strictly related to internal structural constraints or transient secondary structures of the strands (e.g., hairpin-like conformations) [46]. As a final confirmation of the quality of the model, the trend has also been reproduced using the corresponding linear equation (Fig. 2a, bottom right insert), thus confirming the adequacy of the adopted first kinetic order fit for the hybridization reaction.

The same phenomenon has been analyzed on ssDNA-MDs system, following the donor signal, as shown in Fig. 2b. In this case, acquisition of the Cy5 emission was not possible due to its quenching, which can be ascribed to the presence of Br^- in solution [47] as counterion of the DDAB quaternary ammonium group. In fact, the heavy atom effect of Br^- can quench the acceptor fluorescence when the duplex forms on the MDs surface, depending on the fluorophore excited-state lifetime (τ_0), as described by Stern-Volmer equation [47,48]. Accordingly, the quenching effect is greater for Cy5 ($\tau_0 = 1$ ns) [49,50], than for Cy3 ($\tau_0 = 0.2$ ns) [51], jeopardizing the observation of FRET (see SM, section S1.5, Fig. S10). Hence, the data were fitted using the monoexponential model applied to Cy3 emission signal, giving an apparent kinetic rate constant of $k_1 = (21.9 \pm 0.2) \times 10^{-4}$ s^{-1}. In this case, the fitting model has been selected considering that the complementary hybridization process occurs on a densely DNA-functionalized interface (DNA coverage degree is approximately 70% as determined in SM, section S1.3, Fig. S7 and S8). This implies that the density of immobilized probes remains high and essentially constant throughout the association events, while the concentration of the complementary target in solution changes only as the hybridization proceeds. Under these conditions, the measured fluorescence can be appropriately described by a pseudo-first-order exponential model. Finally, comparison of the two apparent kinetic rate constants indicates that the hybridization process occurs within the same order of magnitude, confirming duplex formation on MDs surface. The apparent association rate constant at the interface matches or even more than doubles that observed for free ssDNAs in bulk, bypassing typical transport, orientational, and steric limitations [52]. This behavior is probably driven by an electrostatic steering mechanism sustained by the net positive charge of the lipid shell (+24 mV), as interface-bound DNA hybridization kinetics are known to be significantly modulated by electrostatics and surface-induced orientation [53]. Furthermore, the interfacial probe decoration may provide an extended, binding-ready configuration, preventing probe hairpin self-folding due to the strong interaction of the phosphate backbone with the cationic lipid surface.

3.3. ssDNAs binding affinity on MDs surface

In order to determine the binding affinity of the ssDNAs hybridization process, expressed as the equilibrium dissociation constant K_{obs}, emission spectra of both free and MDs-bound ssDNA-Cy3 were acquired at a fixed donor concentration while titrating with increasing amounts of ssDNA-Cy5. For each condition, the maximum emission value was subtracted to the maximum intensity of ssDNA-Cy3 alone and plotted as a function of ssDNA-Cy5 concentration, resulting in hyperbolic curves.

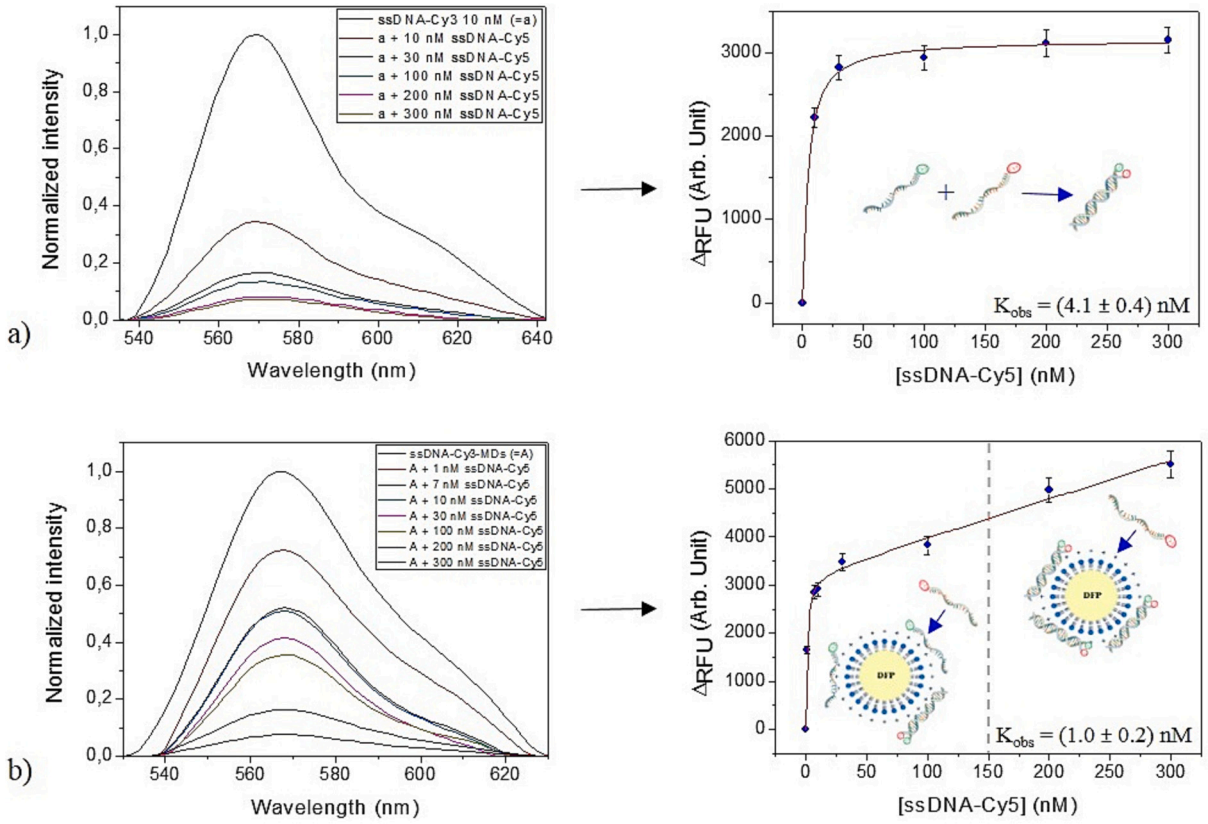


Fig. 3. Emission spectra of ssDNA-Cy3 alone and in presence of increasing [ssDNA-Cy5] (left) and hyperbolic curve derived from fluorescence spectra with its fitting (right): panel a) 10 nM ssDNA-Cy3 is named "a", K_{obs} = (4.1 ± 0.4) nM; panel b) 20 nM ssDNA-Cy3 + 2•10^6 MDs/ml (1:1; named as "A"), K_{obs} = (1.0 ± 0.2) nM. Dashed gray line is a guide for the eye. All the experiments were performed in PBS according to section 2.5.

These data were fitted using eqs. (2) and (3) (Materials and Methods, section 2.5) for the free and MDs-bound processes, respectively, as shown in Fig. 3. Specifically, in the case of free ssDNAs (Fig. 3a, left) the fluorescence donor intensity decreased progressively upon the addition of csDNA-Cy5, consistent with the FRET phenomenon and confirming the hybridization. The corresponding Langmuir isotherm (Fig. 3a, right) yielded a K_{obs} of 4.1 ± 0.4 nM, indicating high binding affinity [54,55]. For the MDs-bound system (Fig. 3b, left), the donor fluorescence intensity likewise decreased as the cs-DNA-Cy5 concentration increased due to FRET, demonstrating that hybridization occurs also on the MDs surface. The corresponding equilibrium dissociation constant was derived by fitting the resulting curve (Fig. 3b, right) with the approximated eq. (3), which accounts for both complementary strand hybridization and competitive adsorption of ssDNA-Cy5 onto the free MD surface (see SM, section S1.6). After establishing that this additional interaction occurs at a significantly higher concentration (μM vs nM range; see SM, section S1.6, Fig. S11), the model was applied to reproduce the experimental trend, resulting in a value of K_{obs} = 1.0 ± 0.2 nM. Further, the statistical analysis of the fitting procedure (SM, section S1.6, Table S1 and Fig. S12) strongly corroborates the quality and robustness of the adopted equation in describing the experimental trend and deriving the constant value.

The comparison between the two K_{obs} values suggests that the high binding affinity of the DNA pairing is maintained also when the process occurs in the MDs-aqueous medium. More importantly, the fact that the affinity remains consistently within the nanomolar range provides definitive proof that the target strands are captured directly on-site at the soft interface, where the high positive surface charge density efficiently hosts the newly formed duplexes. Such an on-site hybridization process has been extensively validated for DNA-decorated lipidic interfaces [53,56,57]. According to the literature, hybridization at such interfaces is quite robust and could be less favorable with respect to the same reaction taking place in solution. Generally, the efficiency of the process is influenced by interface-related constraints, for instance electrostatic repulsion, steric hindrance and nonspecific adsorption of DNA strands on the surface [58]. In our case, we assume that these factors did not significantly affect the binding affinity, as we obtained comparable K_{obs} values in both conditions. Likely, this effect is due to the optimization of the probe surface density and DDAB-DNA ratio, limiting and screening of inter-strand phosphate repulsions on the electrostatically active interfaces [53,59] in which highly positive cationic matrices effectively "trap" and stabilize the incoming target. In fact, the measured 70% DNA-coverage degree, corresponding to approximately 10^6 ssDNAs/MD (see SM, section S1.3, Figs. S7 and S8), provides a sufficient density of accessible hybridization sites, while maintaining the system in a colloidal stability regime (ζ ~ +24 mV). Therefore, the obtained K_{obs} value reflects the hybridization process occurring at an interface with an optimized functionalization density rather than a limitation arising from insufficient or exceeding DNA loading; and is supported by an independent experimental quantification of the DNA surface loading and accessibility. Even the nonspecific adsorption contribution is limited, being the affinity of the ssDNA-Cy5 adsorption onto the free MD surface significantly lower with respect to the hybridization mechanism, thus not competitive, as we demonstrated (see SM, section S1.6). Further, at 25 °C DDAB hydrophobic chains adopt a tightly packed crystalline phase, with a high surface charge density due to polar heads arrangement [26]. Because of this organization, we suppose that the DNA strands are not being buried inside the MDs structure, thus remaining available on the outer shell for hybridization.

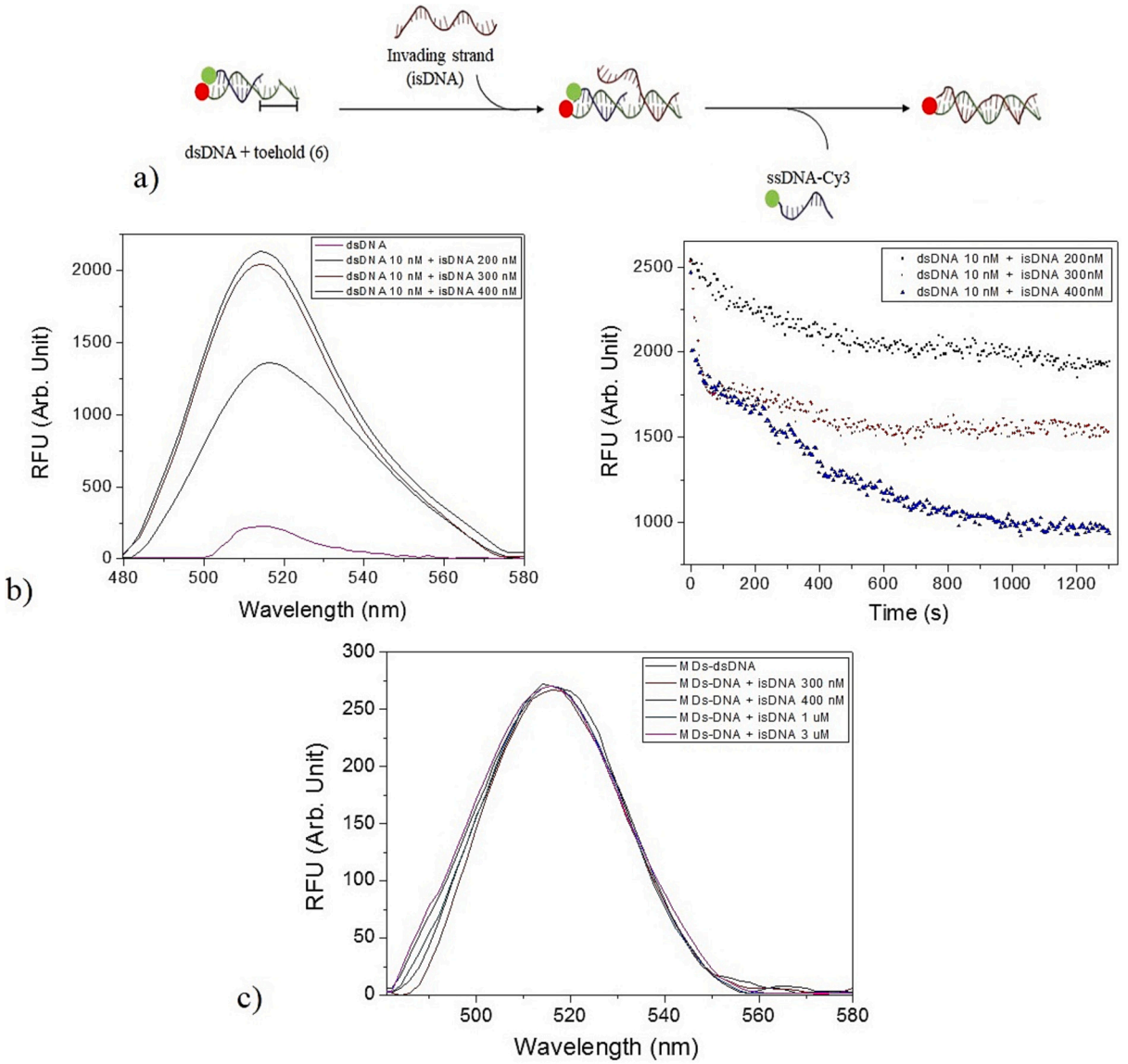


Fig. 4. Strand displacement reaction: a) schematic representation of the reaction mechanism b) donor emission spectra of a 10 nM dsDNA solution measured at increasing [isDNA] 15 min after the mixture of the reactants (left) and corresponding FRET signal (right) c) emission spectra of Cy3 in a pre-formed system of 20 nm dsDNA +2 × 10^6 MDs/ml (1:1) after 15 min from the addition of different [isDNA]. All the experiments were performed in PBS according to section 2.6.

3.4. Strand displacement reaction on MDs surface

The occurrence of DNA strand displacement reactions on MDs surface was explored as potential mechanism to enable sequential DNA hybridizations on the platform shell. The phenomenon was evaluated in solution on free dsDNA and on dsDNA-MDs using a non-modified isDNA, complementary to ssDNA-Cy5, featuring a 6-nt toehold (Fig. 4a). For free dsDNA, displacement was tracked through donor and FRET emission, as hybridization of the isDNA with ssDNA-Cy5 releases ssDNA-Cy3, causing increased Cy3 fluorescence and decreased FRET efficiency (Fig. 4b). Among the different tested concentrations, 300 nM isDNA was selected (Fig. 4b, red curves), which provided an optimal balance between effective displacement, signal clarity and DNA usage, and was further employed in cellular experiments. The same assay performed on dsDNA immobilized at the MDs surface showed no detectable changes in donor emission spectra up to 3 μM isDNA (Fig. 4c), indicating that strand displacement does not occur on the MDs. At the MDs interface, this likely results from reduced accessibility to the invader of the toehold, whose length affects the displacement reaction speed [38,60].

3.5. Study of selective coalescence between ssDNA-MDs

To verify whether ssDNAs hybridization on MDs surface could induce their selective coalescence, the DNAs interaction on MDs was further characterized via DLS analysis. A schematic representation of the proposed interaction mechanism is illustrated in Fig. 5a. The complementary DNAs used had identical sequences to those employed in the previous analysis, but were unlabeled. The MDs size distributions were assessed for four different populations: A (ssDNA-MDs), B (csDNA-MDs), A + A (1:1, non-specific coalescence control), and A + B (1:1, selective coalescence). Acquisitions of each sample were carried out every 30 min and after 2 h of incubation the measured size was stable. The obtained results are reported in Fig. 5b and Table 1.

As shown in Fig. 5b and Table 1, after 2 h from the mixing of A and B, the resulting population A + B has doubled the original size (~ 2.5 μm) reaching a mean diameter of 5.6 ± 0.5 μm, consistent with what expected by the coalescence theoretical model [21]. Under identical conditions, the control sample (A + A) showed no significant increase in the average size (2.8 ± 0.4 μm). These findings indicate that the selective

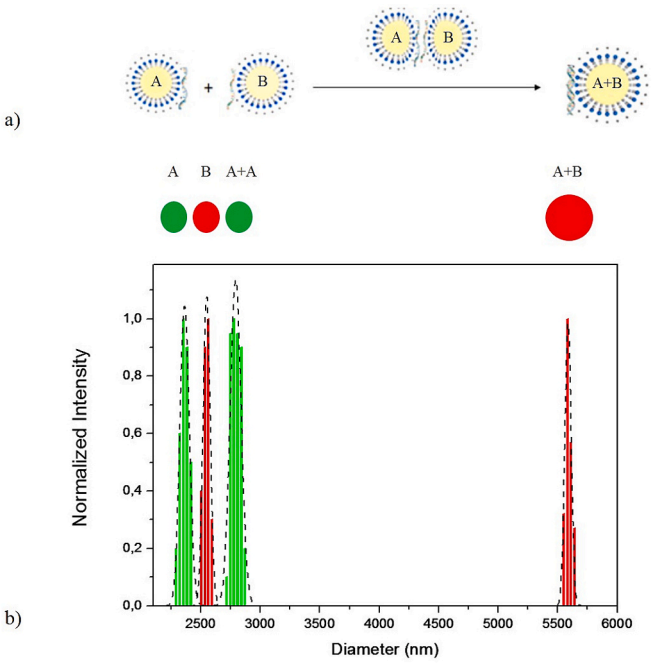


Fig. 5. a) Schematic representation of selective MDs coalescence mechanism induced by complementary DNA strand hybridization b) DLS size distributions of population A (ssDNA-MDs), B (csDNA-MDs), A + A (nonspecific coalescence) and A + B (specific coalescence). All measurements were performed in PBS according to section 2.8.

Table 1
Average diameters of each population measured 2 h after the mixing of the system components.

Sample	Average diameter (2 h, μm)
A	2.4 ± 0.2
B	2.6 ± 0.3
A + A	2.8 ± 0.4
A + B	5.6 ± 0.5

coalescence (A + B) is more efficient than the non-specific one (A + A), which occurs to a minimal extent and on a longer time scale, exhibiting slower kinetics. A + A and A + B share the same MDs formulation, DDAB concentration, DNA surface density and decoration protocol; thus non-specific mechanisms such as surface destabilization, charge neutralization or just the presence of adsorbed DNA should affect both systems similarly. Further, all coalescence experiments were performed in the same buffer (PBS 0.01 M, pH 7.4), whose dilution was selected to limit salt-related effects on the colloidal stability due to electrostatic screening. Therefore, differences between A + A and A + B cannot be attributed to variations in salt concentration, being ionic strength conditions ensured to be identical for both MDs populations. The only experimental variable in which the two populations differ is the DNA sequence and so the ability of the complementary DNA strands in A + B to hybridize. Therefore, we justify this dissimilar behavior as a consequence of the complementary DNAs hybridization on the MDs surface, and we conclude that the increased coalescence observed exclusively for A + B group is related to sequence-specific-induced MDs fusion. This interpretation is also supported by the fluorescence experiments for binding affinity (Fig. 3), which demonstrate that immobilized DNA onto the MDs surface still retains high hybridization affinity. In both cases (A + A and A + B), the ssDNA coating reduces the MDs surface charge associated with DDAB quaternary ammonium, decreasing the ζ-potential from ~ + 78 mV to ~ + 24 mV (see SM, section S1.1, Fig. S3 and section 1.2, Fig. S6) and making the system less stable against coalescence phenomena. However, for the A + B population, DNA complementarity extends the contact time between the MDs, promoting a specific and more rapid coalescence [21]. This interaction results in the formation of bigger drops within approximately 2 h, whereas bare MDs reach comparable sizes only after six days from the synthesis (see SM, section S1.1, Fig. S2f).

The coalescence kinetics were further investigated via CLSM analysis on ssDNA-MDs containing fluorophores (population A: ssDNA-BODIPY-FL-MDs and population B: csDNA-Nile-Red-MDs), chosen according to their hydrophobicity to be incorporated in the MDs core. The aforementioned probes mimic reagent entrapment in the MDs, such as drugs or hydrophobic molecules, and enable FRET upon coalescence. Also in this case, unlabeled ssDNAs were employed to prevent the spectral overlapping of fluorescence emissions. Fig. 6a shows a scheme of the ssDNA-fluorophore-MDs arrangement and the corresponding CLSM micrographs for both populations. Upon mixing A and B populations within an IBIDI μ-Slide 4 well, images (derived from time-lapse videos) revealed selective coalescence with MDs increasing in size (Fig. 6b) and exhibiting a significant green-to-red emission shift, due to FRET (i.e. BODIPY acts as donor and Nile-Red as acceptor). Further, selective coalescence was already evident within the first 6 min after the mixing of A and B, while non-specific coalescence occurred only to a negligible extent. These findings highlight that the hybridization of DNA complementary strands drives coalescence faster and in a more efficient way compared to non-specific interactions.

Starting from the first and last time-lapse frames, microscopy-based size distribution at t_0 (before A + B mixing) and $t = 6$ min (at the end of the coalescence video) were derived, as shown in Fig. 6c. The analysis revealed an increase in the MDs average diameter at $t = 6$ min, from 2.5 ± 0.6 μm for A to 3.3 ± 0.9 μm for A + B, as a consequence of coalescence events. As can be seen from the reported graphs, the final size distribution remained asymmetrical and broader, including a residual population of smaller droplets. Further, the mean diameter resulted smaller than that measured by DLS (Fig. 5 and Table 1). This is expected, as the microscopy analysis captures only the early stages of the coalescence process, being performed on a 6-min acquisition video; whereas DLS measurements were executed after 2 h of incubation of A + B. Therefore, it is likely that sequential coalescence events occurred during that extra time and contributed to shift the DLS population toward larger droplets. Overall, these observations provide a coherent picture of the coalescence, which evolves from predominantly binary events in the early stages of the process (captured by microscopy) to multiple sequential fusions over longer incubation times (up to around 10 initial droplets according to DLS measurements). In addition to time-dependent factors, the differences of microscopy-derived size distributions, which are slightly broader than the corresponding DLS profiles, are also due to the used techniques for the analyses. In fact, microscopy measured the geometric diameter of a limited number of individual droplets in a selected field of view (number-based distribution); while DLS provided an ensemble-averaged intensity-weighted hydrodynamic size distribution over the entire sample (thereby emphasizing the contribution of larger droplets).

Moreover, starting from the time-lapse videos, mean fluorescence intensities of both, red and green channels, were measured on different frames and the curves reported in Fig. 6d were obtained. As shown in the graph, our results demonstrate a progressive increase of the red fluorescence with a corresponding decrease of the green signal, quantitatively confirming FRET occurrence due to MDs cores mixing after coalescence. The quantitative analysis corroborates the qualitative observations reported in the representative confocal images and demonstrates that the fluorescence redistribution is strictly related to the coalescence process.

Finally, we tested whether the yield and frequency of coalescence events could be boosted using a microfluidic setup, as illustrated in Fig. 7. The MD populations (A and B, as in the former experiment) were injected separately into an IBIDI μ-Slide III ^{3in1} channel at a controlled

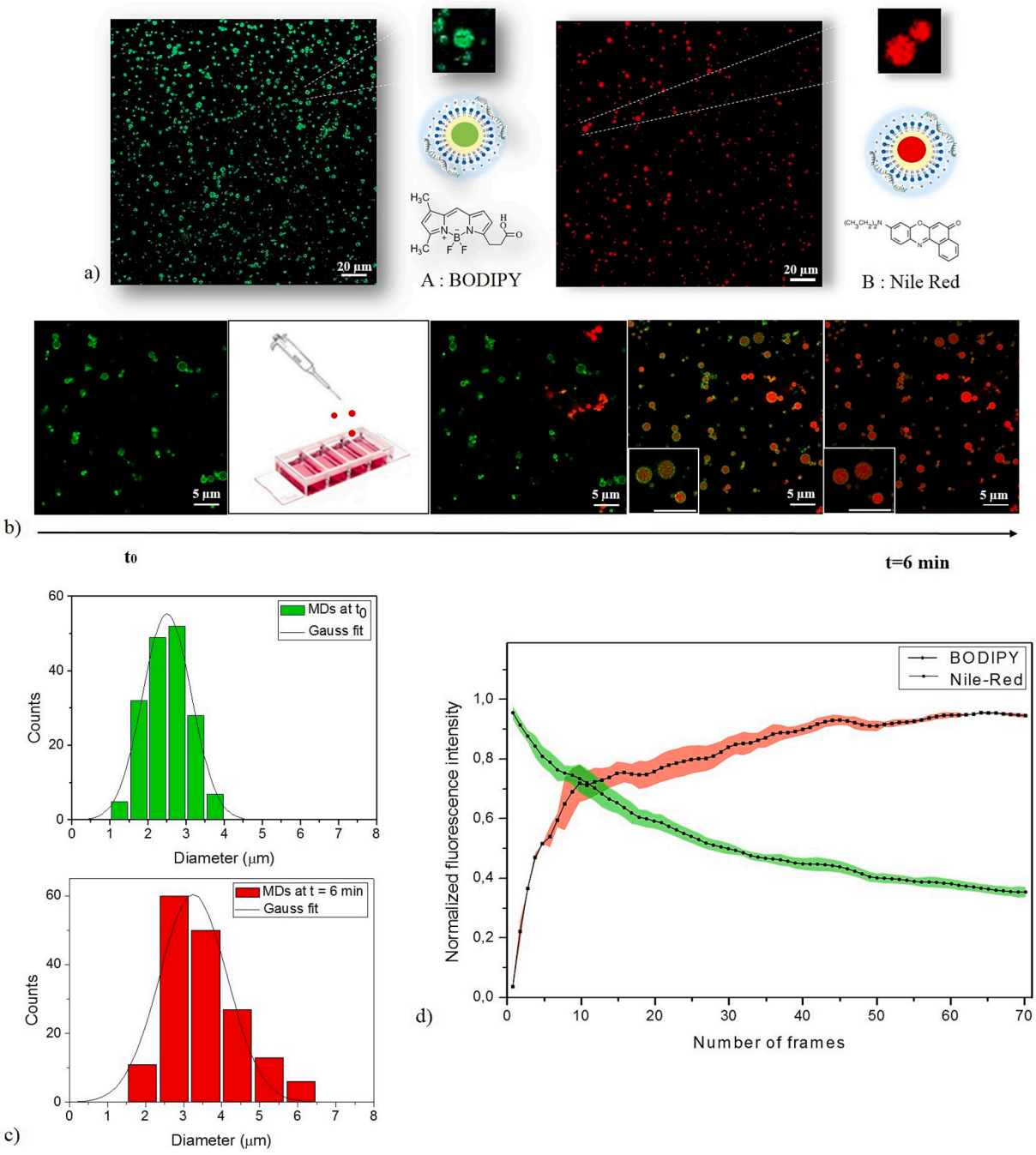


Fig. 6. Selective coalescence CLSM experiment and analyses. Confocal images of ssDNA-MDs with fluorescent dyes inside the DFP core: a) population A: ssDNA-BODIPY-MDs (left) and population B: csDNA-Nile-Red-MDs (right); objective 60×, scale bar 20 µm; b) representative micrographs from time lapse video of real time coalescence in IBIDI µ-Slide 4 well. Bottom left: zoom of MDs involved in coalescence event. Objective 60×, scale bars 5 µm. All the experiments were performed in PBS according to section 2.8; c) microscopy-based size distribution of MDs before (t_0, upper graph) and during coalescence (t = 6 min, lower graph); d) mean fluorescence intensity analysis of green (BODIPY) and red (Nile-Red) channels derived from time-lapse videos frames. (For interpretation of the references to colour in this figure legend, the reader is referred to the web version of this article.)

flow rate, sufficiently fast to ensure effective contact between the droplets while preventing separation and bouncing phenomena [19,21].

The flow behavior was monitored by CLSM, and time-lapse videos were recorded under steady-state conditions (representative frames are shown in Fig. S13, Section S1.7, SM). In particular, in a representative experiment fixing the flow at 0.89 ml/min, the trajectory analysis allowed us to resolve distinct kinematic populations, yielding the estimated fraction (%) of coalesced droplets, the mean velocity ($\bar{v}$) of the non-interacting population, and a characteristic velocity ($\bar{v}_{coalescence}$) that we associated with the droplet subpopulation undergoing coalescence (i.e., coalescing phase). These parameters, alongside the mean diameter ($\bar{d}_{product}$) of the particles collected at the outlet after approximately 5 s for DLS analysis, are summarized in Table 2.

The coalescence efficiency was substantially higher for the specific A + B condition (87%, where droplets are decorated with complementary DNA strands) than for the non-specific A + A control (6%), confirming that the phenomenon is driven by selective DNA hybridization. To highlight this behavior, the corresponding velocity distributions and 2D

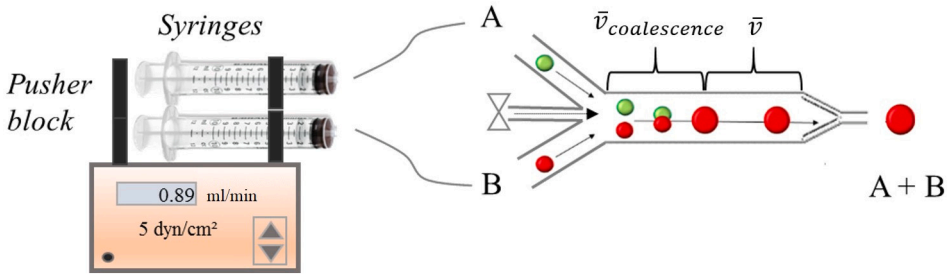


Fig. 7. Microfluidic setup designed to boost coalescence events: two syringes with a pump are used to inject separately each MDs population in an IBIDIμ-Slide III ^{3in1} channel (injection rate = 0.89 ml/min, shear stress = 5 dyn/cm^2).

Table 2
MDs trajectory parameters derived from the coalescing time-lapse videos and mean size of the resulting coalescence product from DLS measurements.

	Non-specific coalescence (A + A)	Specific coalescence (A + B)
Coalescence events	~6%	~87%
$\bar{v}_{coalescence}$ (μm/s)	23 ± 7	34 ± 12
$\bar{v}$ (μm/s)	136 ± 21	138 ± 35
$\bar{d}_{product}$ (μm)	2.9 ± 0.4	5.3 ± 0.3

diameter-velocity cluster plots were shown and discussed in detail in Section S1.7 and Fig. S14 of SM. In the A + A control, the droplets exhibited a broad, highly dispersed velocity profile spanning a wide range without displaying a single prominent peak, with $\bar{v}$ = 136 ± 21 μm/s. Conversely, the interactive A + B system displayed a single main log-normal distribution centered around a low-velocity peak, accompanied by a tail of faster droplets (Fig. S14c, SM).

In the 2D cluster plot (Fig. S14d, SM), a velocity threshold at 90 μm/s was used to separate the faster droplets from the main population, which correlates with the equivalent diameters of the coalesced particles. The population in the high-velocity regime maintained a $\bar{v}$ of 137.7 ± 35.4 μm/s, consistent with the control. This value confirms the hypothesis that within this high-velocity regime no coalescence events occur (regardless of whether the droplets underwent a prior fusion event before accelerating). On the other hand, averaging the tracking data below the 90 μm/s threshold yielded a characteristic $\bar{v}_{coalescence}$ of 34 ± 12 μm/s. This value is in agreement with the modal peak of the log-normal distribution (37.4 ± 15.6 μm/s) obtained by isolating the larger coalesced droplets (d > 2.8 μm) within this low-velocity regime. Indeed, a significant reduction in the resultant velocity is expected due to the transient hydrodynamic and viscous changes associated with the coalescence event. As corroborated by DLS measurements (Table 2), these data (the MDs size increase and reduced velocity) demonstrate that specific DNA-DNA recognition enables sustained droplet contact under the chosen microfluidic setup conditions, triggering a more efficient selective fusion.

3.6. Cytotoxicity evaluation by MTT assay

The cytotoxicity of the MDs, unlabeled-ssDNA, and DNA-MDs systems was determined on SK-MEL-28 cell line using MTT assay to evaluate their suitability for biological applications. As shown in Fig. 8, cell viability (%) for MDs (Group A) and ssDNA-MDs (Group B) decreased slightly with increasing MDs concentration, but remained above 90%, which is considered safe. Only the highest concentration tested reduced viability below 80%, likely due to excessive MDs density hindering nutrient diffusion to the cells. Regarding the ssDNA treatments (Group C), in each condition, cell viability stayed invariable and roughly comparable to the control sample within the error, indicating that the ssDNA sequences used are not cytotoxic. With this background, 0.55 nM ssDNA +3.3 × 10^7 MDs/ml (Group B, condition 3) was selected as the optimal concentration for subsequent transfection experiments on tumor cells, as it preserved cell viability while allowing efficient ssDNA delivery.

3.7. Tumor cell DNA – Transfection

Following the characterization and cytotoxicity assessment, we evaluated ssDNA-MDs potential as DNA transfection vector into human melanoma SK-MEL-28 cell line, a model chosen for its clinical relevance. Metastatic melanoma is a cancer derived from melanocyte and has

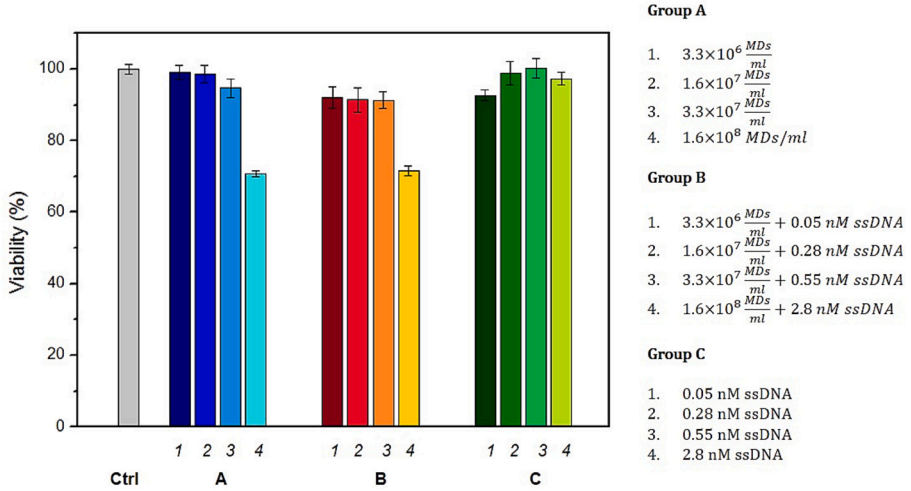


Fig. 8. Percentage of cell viability of the different tested conditions obtained from the MTT assay.

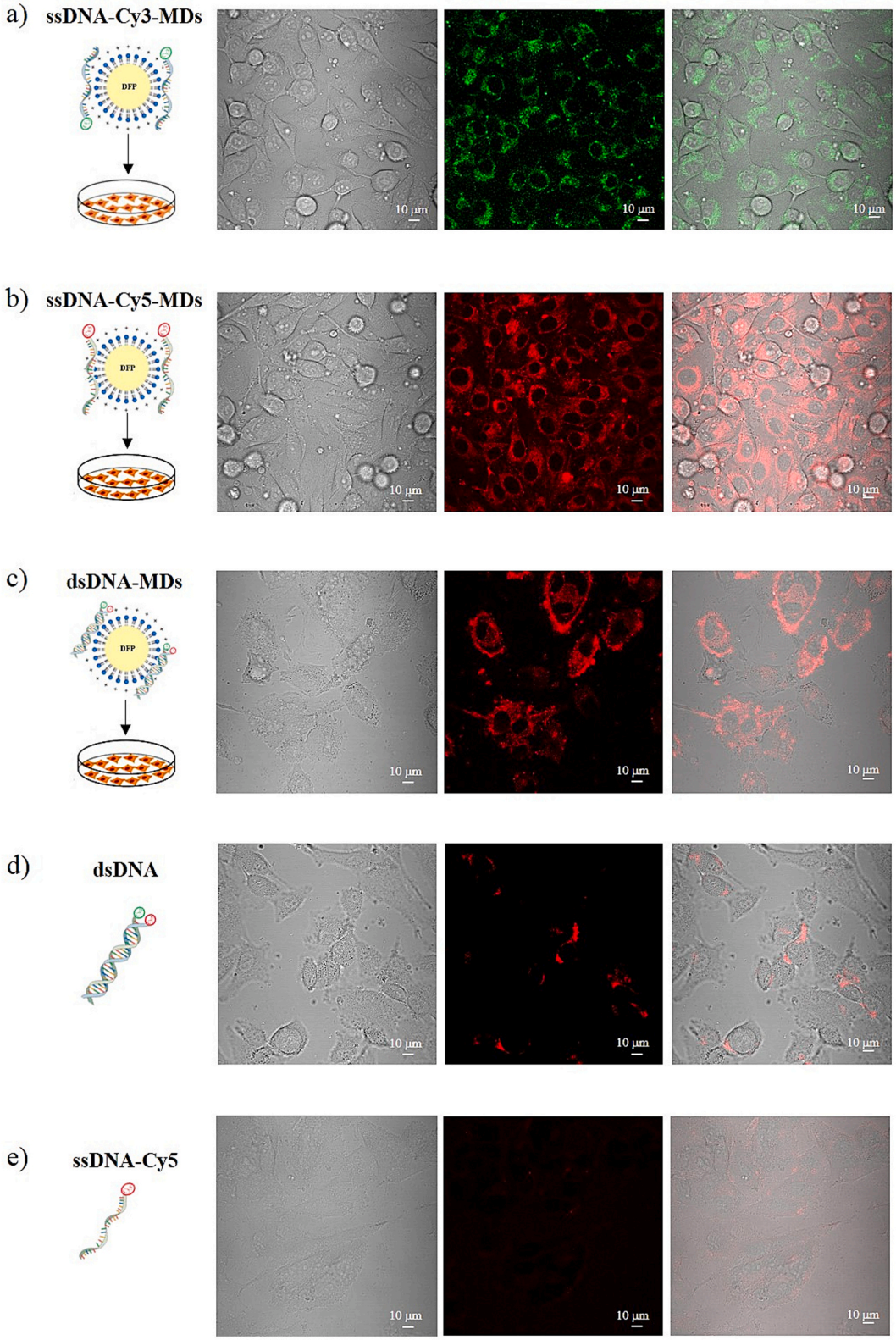


Fig. 9. Confocal images of SK-MEL-28 cells treated with ssDNA-MDs (a, b), dsDNA-MDs (c), dsDNA (d) and ssDNA-Cy5 (e). For each treatment from the left: transmission image, the respective fluorescence micrograph due to Cy3 (green) or Cy5 (red) 2 h after treatment, and merge. Objective 60×, scale bar 10 μm. (For interpretation of the references to colour in this figure legend, the reader is referred to the web version of this article.)

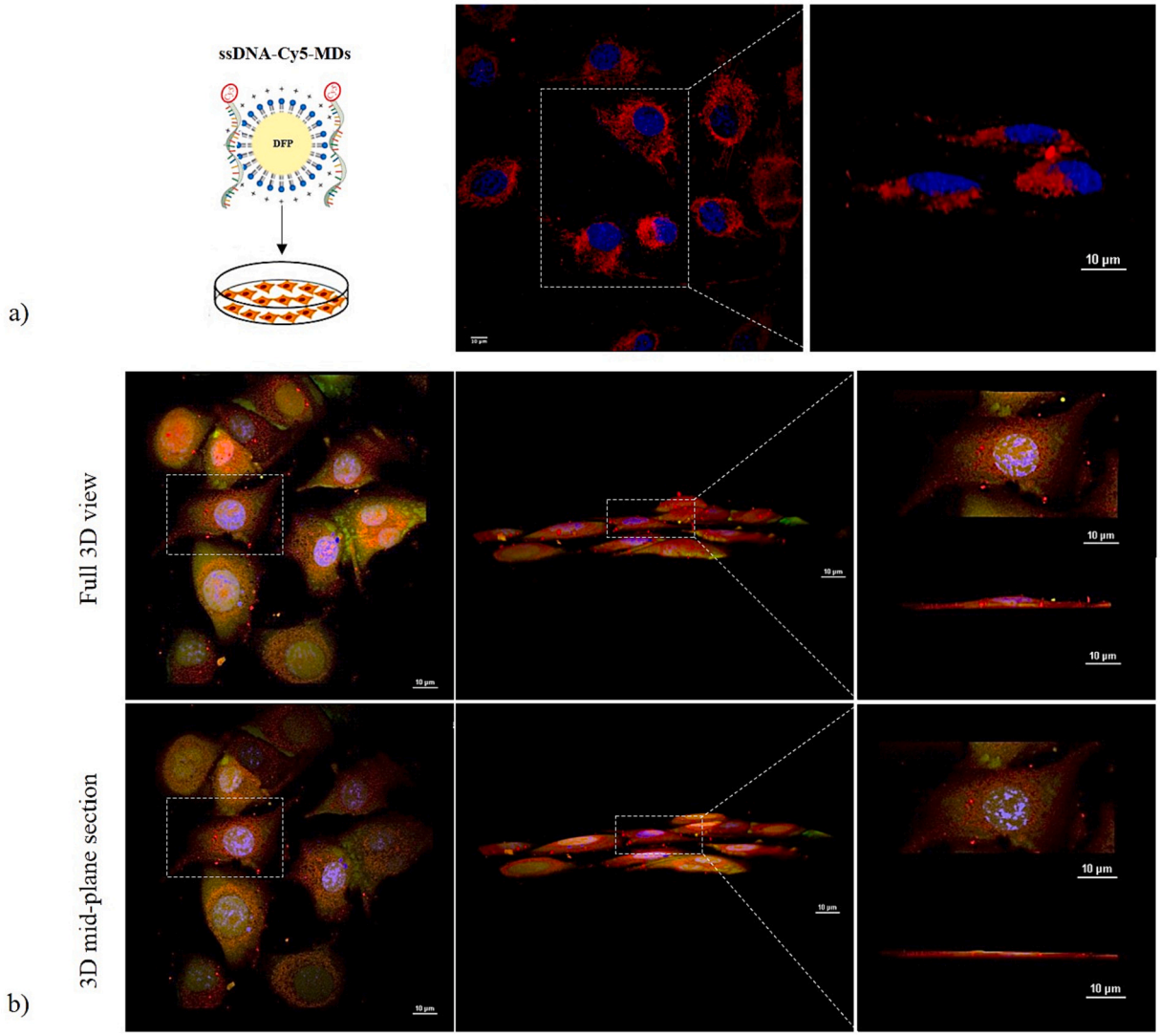


Fig. 10. Representative images of DNA distribution in SK-MEL 28 after 2 h treatment with ssDNA-Cy5-MDs: a) 2D confocal image of cells, Hoechst-stained nuclei (blue) and ssDNA-Cy5 (red); 3D confocal reconstruction of dashed selection; b) 3D confocal reconstructions of cells labeled with Calcein-AM (green), Hoechst (blue) and ssDNA-Cy5 (red). Top: full tridimensional views in different projections and zoom of dashed selection. Bottom: 3D mid-plane section of upper panel and corresponding zoom. Objective 60×, scale bars 10 µm. (For interpretation of the references to colour in this figure legend, the reader is referred to the web version of this article.)

limited treatment options. Since the most common mutations in melanomas are activators in BRAF and MAPK, transfection of mature RNA can regulate the expression of the target protein by coupling with their mRNAs. This occurs by inducing translational repression and/or degradation of mRNA [61]. As discussed above (section 3.6), we performed our experiments at the concentration of 0.55 nM ssDNA +3.3 × 10^7 MDs/ml, selected on the basis of the MTT assay results. After 2 h-incubation with ss or dsDNA-MDs, the cells were washed to remove unbound MDs and free DNA, and analyzed by CLSM (Fig. 9). Emission monitoring of Cy3/Cy5 linked to the ssDNAs sequences and FRET signal confirmed intracellular localization of the transfected DNA in the cytosol, without nuclear membrane penetration (Fig. 9a-c). Conversely, dsDNA delivered without MDs showed minimal uptake and peripheral aggregation in the cellular environment (Fig. 9d). A similar distribution, even if less evident, is observed for ssDNA-Cy5 alone (Fig. 9e). These findings suggest that MDs are not internalized in the cells, but instead act as a scaffold, with the real transfecting agent being the DDAB forming the droplet shell. Indeed, due to its amphiphilic nature, which makes it affine for the cellular membrane, DDAB has been widely used for DNA delivery into cells both in vitro [62–64] and in vivo [65,66]. Additionally, it has been proved to be an efficient carrier for genes and drugs as a component of cationic liposomes [64,67] or polymeric nanoparticles [63,64,67,68]. Hence, we suppose that the DDAB shell of MDs directly interacts with the cell membranes by releasing the DNA and making it enter the cells over a time scale of about two hours.

To further investigate the ability of MDs to transfect DNAs inside the cells and the subsequent intracellular distribution, SK-MEL 28 nuclei were labeled with Hoechst dye and *Z*-stack images were acquired (Fig. 10a). As previously suggested in Fig. 9, we confirmed that the DNA remains confined in the cytosol without nuclear internalization, as revealed by ssDNA-Cy5 signal (red) localization near the nuclei. In order to better understand DNA compartmentalization in live cells, SK-MEL 28 cells were stained with Calcein-AM fluorophore, allowing visualization of the cellular cytoplasm (Fig. 10b). In the 3D-stacks of the cells, it is possible to distinguish between membrane-associated red fluorescence, generated by ssDNA-Cy5 outside the cell, and inner emission, given by internalized DNA. Our results (Fig. 10b, upper lane) suggest that the ssDNA-Cy5 signal outside the cells is negligible with respect to the intracellular amount. Further, to assure that the DNA delivery was accomplished, starting from full 3D view images, the 3D mid-plane

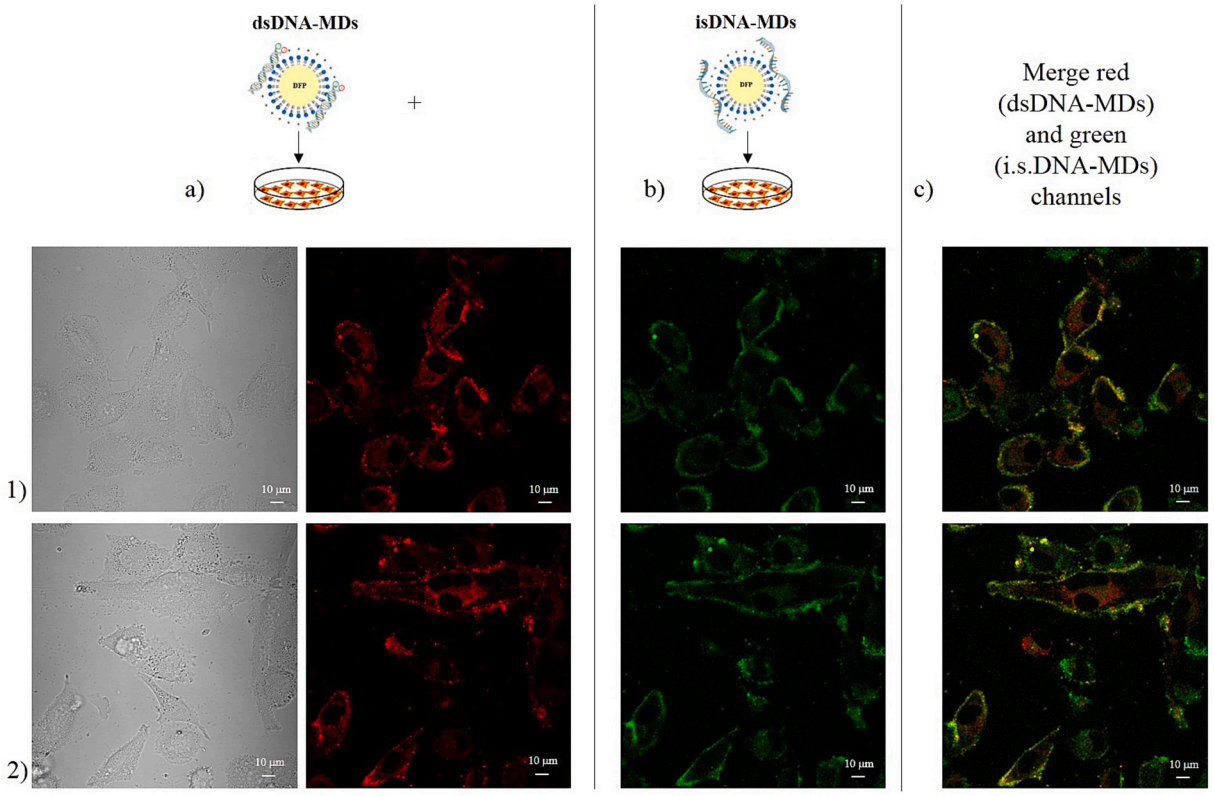


Fig. 11. CLSM images of SK-MEL-28 cells (a) after 2 h of incubation with dsDNA-MDs and (b) following the addition of isDNA-MDs for 45 min; c) strand displacement reaction: decrease of FRET phenomenon in merged images of red and green channels. Objective 60×, scale bar 10 μm. (For interpretation of the references to colour in this figure legend, the reader is referred to the web version of this article.)

section (Fig. 10b, lower panel) of the previous micrographs was selected. As it is appreciable from the images, the ssDNA-Cy5 red signal remains detectable inside the cells, thus demonstrating efficient transfection inside the cells.

To verify whether DNA is able to enter the cell without remaining bound to the MD carrier, we tested if a strand displacement reaction could occur inside the cells, performing two sequential transfections. SK-MEL-28 cells pre-treated with dsDNA-MDs were incubated with isDNA-MDs for 45 min. Again, we monitored the cyanine emissions via CLSM after multiple rinses (Fig. 11). The acquired images in panel a) show the internalized dsDNA in SK-MEL-28 after 2 h of treatment, consistent with the previous observations in Fig. 9c. The micrographs in Fig. 11b highlight that the isDNA has been uptaken by the cells as well, leading to a shift emission toward green, indicating strand displacement occurred. As discussed earlier (section 3.4, Fig. 4c), this reaction does not take place on MDs surface, likely due to steric hindrance. Thus, we conclude that the displacement occurred in solution, involving the free DNAs released from the MDs into the cells. Furthermore, merged images (Fig. 11c) reveal that in 45 min the reaction has mainly completed proximal to the cell membrane. In fact, deeper regions of the cells still showed residual FRET signal (Cy5 emission), demonstrating that in those areas the displacement has not occurred yet. This finding supports our proposed mechanism for the DNA transfection, in which the MDs DDAB shell is supposed to interact with the cell membrane and mediate DNA release, leading at first to a higher local DNA concentration near the membrane. Moreover, we can affirm that in the time span of both treatments (approximately 3 h), the internalized DNAs were not degraded by any cell mechanism, as the strand displacement reaction took place.

4. Conclusions

Based on a previously reported approach for the synthesis of DDAB-DFP MDs [15], this study demonstrates the successful engineering of this system with complementary ssDNAs, establishing a responsive colloidal platform capable of selective, DNA-driven coalescence. Moreover, exploiting the well-known properties of DDAB as a DNA delivery lipid vector [64,66,67], we also explored the invaluable potential of DDAB-DFP MDs as a transfection agent in human tumor cells.

To this end, we first defined the formulation, physicochemical properties, and working conditions of the MDs and DNA composing the colloidal system, followed by a detailed study of their interaction and stability at the aqueous interface, which was lacking in the literature. The present work has successfully addressed this gap. Using FRET-based analyses on distinct cyanine-labeled complementary DNAs, we demonstrated that duplex formation occurs on the MDs surface as well, maintaining both high binding rate and affinity. This is a key feature to ensure that the reaction remains kinetically efficient and thermodynamically favorable enough to be exploited for tailoring coalescence between different MDs populations.

The high affinity of ssDNAs complementary hybridization was shown to trigger selective coalescence events between distinct fluorophores-loaded MD populations, validated by quantitative CLSM FRET studies and DLS analyses, resulting in droplet fusion and core content mixing. Moreover, these events occurred on a significantly faster timescale than non-specific coalescence, and could be finely tuned using microfluidic flow to enhance reaction control, also providing kinematic features. Collectively, these findings provide the first experimental evidence that DNA hybridization can be exploited to program colloidal interactions

and induce selective MDs coalescence. More broadly, chemical information drives interfacial selectivity of MDs, directly translating molecular recognition into the controlled mixing of core-encapsulated cargoes. This lays the foundation for the development of programmable microreactors.

Building on this benchmark study, future efforts will focus on optimizing ssDNA designs – such as tunable toeholds [66] – to overcome the restriction that emerged herein in the DNA strand displacement reactions on the droplets surface and enable multistage or sequential coalescence reactions. Such a platform could encapsulate hydrophobic reagents inside the MDs core and generate the desired product upon mixing of distinct MDs populations within aqueous media (e.g., biological fluids).

In parallel, we propose the DDAB-DFP MDs for a second relevant application toward a novel DNA-based technology for DNA transfection into cancer cells. Although non-viral gene therapy is a widely studied research topic, the development of suitable, biocompatible vectors to carry DNA in biological fluids faces several issues in terms of transport, molecular stability and cell transfection due to the selectivity of the cell membrane [69–72]. Therefore, further in-depth studies are needed in this direction. Our platform demonstrated high biocompatibility (>90% cell viability) over a wide range of concentrations and efficient DNA transfection into SK-MEL 28 cell line without droplet internalization. These features are guaranteed by the stability of the system, the DDAB high affinity for cellular membranes, and the DNA uptake mediated by membrane interaction. Ultimately, confocal FRET imaging revealed that the DNA-MDs vector successfully triggers an intracellular strand displacement reaction. Our findings indicate that this process occurs effectively via free DNA invading strands upon their complete desorption from the lipid shell carrier. The released DNA remains fully accessible and functional, overcoming a major bottleneck of conventional non-viral vectors, where persistent carrier-cargo binding inhibits transfection. Future studies will explore coding DNA delivery, further verified by relative protein expression in cells, including in vivo validation. Bearing also in mind the ability of DDAB-DFP MD to release drugs in tumor cell lines [1,15], the platform may deserve attention as a versatile dual-delivery tool for personalized treatment of genetic disorders and cancer, where coordinated delivery of genes and bioactive molecules may enhance therapeutic efficacy. In this view, programmed coalescence may offer an additional way to deliver pro-drugs and activate them in situ, minimizing side effects and improving therapeutic precision [73,74].

CRediT authorship contribution statement

Giulia Perilli: Writing – review & editing, Writing – original draft, Methodology, Investigation, Formal analysis, Data curation. **Angela Ditri:** Writing – review & editing, Methodology, Investigation, Formal analysis. **Alessandra Vitaliti:** Writing – review & editing, Investigation, Data curation. **Yosra Toumia:** Writing – review & editing, Validation, Supervision. **Alessandro Porchetta:** Writing – review & editing, Supervision, Methodology, Data curation. **Gaio Paradossi:** Writing – review & editing, Validation, Supervision, Resources. **Fabio Domenici:** Writing – review & editing, Writing – original draft, Supervision, Resources, Methodology, Investigation, Formal analysis, Conceptualization.

Declaration of competing interest

The authors declare that they have no known competing financial interests or personal relationships that could have appeared to influence the work reported in this paper.

Acknowledgment

Alessandra Vitaliti was supported by Fondazione Umberto Veronesi.

Appendix A. Supplementary data

Supplementary data to this article can be found online at https://doi.org/10.1016/j.jcis.2026.141646.

Data availability

Data will be made available on request.

References

[1] D. Palmieri, F. Brasili, A. Capocefalo, T. Bizien, I. Angelini, L. Oddo, Y. Toumia, G. Paradossi, F. Domenici, Improved hybrid-shelled perfluorocarbon microdroplets as ultrasound- and laser-activated phase-change platform, Colloids Surf. A Physicochem. Eng. Asp. 641 (2022) 128522, https://doi.org/10.1016/j.colsurfa.2022.128522.

[2] N.P. Pasarkar, M. Yadav, A. Prakash, Mahanwar, A review on the microencapsulation of phase change materials: classification, study of synthesis technique and their applications, J. Polym. Res. 30 (2022) 13, https://doi.org/10.1007/s10965-022-03380-0.

[3] N. Kakaei, R. Amirian, M. Azadi, G. Mohammadi, Z. Izadi, Perfluorocarbons: a perspective of theranostic applications and challenges, Front. Bioeng. Biotechnol. 11 (2023) 1115254, https://doi.org/10.3389/fbioe.2023.1115254.

[4] B.A. Abeid, M.L. Fabiilli, M. Aliabouzar, J.B. Estrada, Experimental & numerical investigations of ultra-high-speed dynamics of optically induced droplet cavitation in soft materials, J. Mech. Behav. Biomed. Mater. 160 (2024) 106776, https://doi.org/10.1016/j.jmbbm.2024.106776.

[5] H. Lea-Banks, M.A. O'Reilly, K. Hynynen, Ultrasound-responsive droplets for therapy: a review, J. Control. Release 293 (2019) 144–154, https://doi.org/10.1016/j.jconrel.2018.11.028.

[6] S. Chaudhary, A. Kaushik, B.A. Abeid, J.B. Estrada, M.L. Fabiilli, M. Aliabouzar, Optical and acoustic characterization of phase-shift droplets with varying Shell compositions, Langmuir (2025), https://doi.org/10.1021/acs.langmuir.4c05030.

[7] F. Huang, J. Zhang, T. Chen, Q. Pan, Z. Zhu, Advancements in manufacturing and applications of multi-dimensional micro-nano materials through interface shearing, Cell Rep. Phys. Sci. 5 (2024) 102033, https://doi.org/10.1016/j.xcrp.2024.102033.

[8] R. Holman, O. Lorton, P.C. Guillemin, S. Desgranges, F. Santini, D.B. Preso, M. Farhat, C. Contino-Pépin, R. Salomir, Perfluorocarbon emulsion enhances MR-ARFI displacement and temperature in vitro: evaluating the response with MRI, NMR, and hydrophone, Front Oncol 12 (2022) 1025481, https://doi.org/10.3389/fonc.2022.1025481.

[9] W. Zhang, H. Metzger, S. Vlatakis, A. Claxton, M.A. Carbajal, L.F. Fung, J. Mason, K.L.A. Chan, A.N. Pouliopoulos, R.A. Fleck, P. Prentice, M. Thanou, Characterising the chemical and physical properties of phase-change nanodroplets, Ultrason. Sonochem. 97 (2023) 106445, https://doi.org/10.1016/j.ultsonch.2023.106445.

[10] G. Calderó, G. Paradossi, Ultrasound/radiation-responsive emulsions, Curr. Opin. Colloid Interface Sci. 49 (2020) 118–132, https://doi.org/10.1016/j.cocis.2020.08.002.

[11] Y. Toumia, M. Pullia, F. Domenici, A. Facoetti, M. Ferrarini, S.V. Heymans, B. Carlier, K. Van Den Abeele, E. Sterpin, J. D'hooge, E. D'Agostino, G. Paradossi, Ultrasound-assisted carbon ion dosimetry and range measurement using injectable polymer-shelled phase-change nanodroplets: in vitro study, Sci. Rep. 12 (2022) 8012, https://doi.org/10.1038/s41598-022-11524-x.

[12] Y. Toumia, R. Miceli, F. Domenici, S.V. Heymans, B. Carlier, M. Cociorb, L. Oddo, P. Rossi, R.M. D'Angellilo, E. Sterpin, E. D'Agostino, K. Van Den Abeele, J. D'hooge, G. Paradossi, Ultrasound-assisted investigation of photon triggered vaporization of poly(vinylalcohol) phase-change nanodroplets: a preliminary concept study with dosimetry perspective, Phys. Med. 89 (2021) 232–242, https://doi.org/10.1016/j.ejmp.2021.08.006.

[13] S. Capece, F. Domenici, F. Brasili, L. Oddo, B. Cerroni, A. Bedini, F. Bordi, E. Chiessi, G. Paradossi, Complex interfaces in "phase-change" contrast agents, Phys. Chem. Chem. Phys. 18 (2016) 8378–8388, https://doi.org/10.1039/C5CP07538F.

[14] P.S. Sheeran, P.A. Dayton, Phase-change contrast agents for imaging and therapy, Curr. Pharm. Des. 18 (2012) 2152–2165, https://doi.org/10.2174/138161212800099883.

[15] E. Tortorella, D. Palmieri, M. Piermarini, D. Gigante, L. Oddo, Y. Toumia, G. Paradossi, F. Domenici, Phase change Dimethyldioctadecylammonium-shelled microdroplets as a promising drug delivery system: results on 3D spheroids of mammalian tumor cells, JoVE (2021) 62255, https://doi.org/10.3791/62255.

[16] S. Mondal, S. Acharya, R. Biswas, B. Bagchi, R.N. Zare, Enhancement of reaction rate in small-sized droplets: a combined analytical and simulation study, J. Chem. Phys. 148 (2018) 244704, https://doi.org/10.1063/1.5030114.

[17] N. Alamoodi, A. Alazzam, Droplet coalescence by selective wettability enhancement in microfluidic devices, Nanomaterials (Basel) 10 (2020) 737, https://doi.org/10.3390/nano10040737.
[18] I. Akartuna, D.M. Aubrecht, T.E. Kodger, D.A. Weitz, Chemically induced coalescence in droplet-based microfluidics, Lab Chip 15 (2015) 1140–1144, https://doi.org/10.1039/C4LC01285B.
[19] C. Tang, P. Zhang, C.K. Law, Bouncing, coalescence, and separation in head-on collision of unequal-size droplets, Phys. Fluids 24 (2012) 022101, https://doi.org/10.1063/1.3679165.
[20] A.H. Brown, C. Hanson, Drop Coalescence in Liquid–Liquid Systems, Nature 214 (1967) 76–77. doi:https://doi.org/10.1038/214076a0.
[21] J. Kamp, J. Villwock, M. Kraume, Drop coalescence in technical liquid/liquid applications: a review on experimental techniques and modeling approaches, Rev. Chem. Eng. 33 (2017) 1–47, https://doi.org/10.1515/revce-2015-0071.
[22] J. Jin, C.H. Ooi, D.V. Dao, N.-T. Nguyen, Coalescence processes of droplets and liquid marbles, Micromachines (Basel) 8 (2017) 336, https://doi.org/10.3390/mi8110336.
[23] J.D. Paulsen, R. Carmigniani, A. Kannan, J.C. Burton, S.R. Nagel, Coalescence of bubbles and drops in an outer fluid, Nat. Commun. 5 (2014) 3182, https://doi.org/10.1038/ncomms4182.
[24] T. Zhang, M. Ding, N. Tao, X. Wang, J. Zhong, Effects of surfactant type and preparation pH on the droplets and emulsion forms of fish oil-loaded gelatin/surfactant-stabilized emulsions, LWT 117 (2020) 108654, https://doi.org/10.1016/j.lwt.2019.108654.
[25] R. Marty, C.N. N'soukpoe-Kossi, D. Charbonneau, C.M. Weinert, L. Kreplak, H.-A. Tajmir-Riahi, Structural analysis of DNA complexation with cationic lipids, Nucleic Acids Res. 37 (2009) 849–857, https://doi.org/10.1093/nar/gkn1003.
[26] F. Domenici, C. Castellano, F. Dell'Unto, A. Albinati, A. Congiu, Silicon supported lipid-DNA thin film structures at varying temperature studied by energy dispersive X-ray diffraction and neutron reflectivity, Colloids Surf. B Biointerfaces 88 (2011) 432–439, https://doi.org/10.1016/j.colsurfb.2011.07.026.
[27] C.M. Panje, D.S. Wang, M.A. Pysz, R. Paulmurugan, Y. Ren, F. Tranquart, L. Tian, J. K. Willmann, Ultrasound-mediated gene delivery with cationic versus neutral microbubbles: effect of DNA and microbubble dose on in vivo transfection efficiency, Theranostics 2 (2012) 1078–1091, https://doi.org/10.7150/thno.4240.
[28] V. Picanço-Castro, C.G. Pereira, D.T. Covas, G.S. Porto, A. Athanassiadou, M. L. Figueiredo, Emerging patent landscape for non-viral vectors used for gene therapy, Nat. Biotechnol. 38 (2020) 151–157, https://doi.org/10.1038/s41587-019-0402-x.
[29] B. Caffery, J.S. Lee, A.A. Alexander-Bryant, Vectors for glioblastoma gene therapy: Viral & non-Viral Delivery Strategies, Nanomaterials (Basel) 9 (2019) 105, https://doi.org/10.3390/nano9010105.
[30] H. Ohshima, Chapter 9 - DLVO Theory of Colloid Stability, in: H. Ohshima (Ed.), Interface Science and Technology, Elsevier, 2024, https://doi.org/10.1016/B978-0-443-16116-2.00009-6, pp. 217–244.
[31] D. Velegol, P.K. Thwar, Analytical model for the effect of surface charge nonuniformity on colloidal interactions, Langmuir 17 (2001) 7687–7693, https://doi.org/10.1021/la010634z.
[32] D. Truzzolillo, F. Bordi, F. Sciortino, C. Cametti, Kinetic arrest in polyion-induced inhomogeneously charged colloidal particle aggregation, Eur. Phys. J. E Soft Matter 29 (2009) 229–237, https://doi.org/10.1140/epje/i2009-10471-1.
[33] F. Brasili, A. Capocefalo, D. Palmieri, F. Capitani, E. Chiessi, G. Paradossi, F. Bordi, F. Domenici, Assembling patchy plasmonic nanoparticles with aggregation-dependent antibacterial activity, J. Colloid Interface Sci. 580 (2020) 419–428, https://doi.org/10.1016/j.jcis.2020.07.006.
[34] A. Amodio, B. Zhao, A. Porchetta, A. Idili, M. Castronovo, C. Fan, F. Ricci, Rational design of pH-controlled DNA strand displacement, J. Am. Chem. Soc. 136 (2014) 16469–16472, https://doi.org/10.1021/ja508213d.
[35] F.C. Simmel, B. Yurke, H.R. Singh, Principles and applications of nucleic acid Strand displacement reactions, Chem. Rev. 119 (2019) 6326–6369, https://doi.org/10.1021/acs.chemrev.8b00580.
[36] S. Ranallo, A. Porchetta, F. Ricci, DNA-based scaffolds for sensing applications, Anal. Chem. 91 (2019) 44–59, https://doi.org/10.1021/acs.analchem.8b05009.
[37] D.Y. Zhang, G. Seelig, Dynamic DNA nanotechnology using strand-displacement reactions, Nat. Chem. 3 (2011) 103–113, https://doi.org/10.1038/nchem.957.
[38] P. Hu, M. Li, X. Wei, B. Yang, Y. Li, C.-Y. Li, J. Du, Cooperative toehold: a mechanism to activate DNA Strand displacement and construct biosensors, Anal. Chem. 90 (2018) 9751–9760, https://doi.org/10.1021/acs.analchem.8b01202.
[39] Y. Piotrowski, M.K. Gurung, A.N. Larsen, Characterization and engineering of a DNA polymerase reveals a single amino-acid substitution in the fingers subdomain to increase strand-displacement activity of A-family prokaryotic DNA polymerases, BMC Mol. Cell Biol. 20 (2019) 31, https://doi.org/10.1186/s12860-019-0216-1.
[40] B. Yurke, A.J. Turberfield, A.P. Mills, F.C. Simmel, J.L. Neumann, A DNA-fuelled molecular machine made of DNA, Nature 406 (2000) 605–608, https://doi.org/10.1038/35020524.
[41] Y. Dai, A. Furst, C.C. Liu, Strand displacement strategies for biosensor applications, Trends Biotechnol. 37 (2019) 1367–1382, https://doi.org/10.1016/j.tibtech.2019.10.001.
[42] I. Langmuir, The adsorption of gases on plane surfaces of glass, mica and platinum, J. Am. Chem. Soc. (1918), https://doi.org/10.1021/ja02242a004.
[43] A. Halperin, A. Buhot, E.B. Zhulina, Hybridization isotherms of DNA microarrays and the quantification of mutation studies, Clin. Chem. 50 (2004) 2254–2262, https://doi.org/10.1373/clinchem.2004.037226.
[44] Z. Yang, Y. Wi, Y. Yoon, P. Verwilst, J.H. Jang, T.W. Kim, C. Kang, J.S. Kim, BODIPY/Nile-red-based efficient FRET pair: selective assay of endoplasmic reticulum membrane fluidity, Chemistry An Asian Journal 11 (2016) 527–531, https://doi.org/10.1002/asia.201501060.
[45] K. Vishwanath, W. Zhong, M. Close, M.-A. Mycek, Fluorescence quenching by polystyrene microspheres in UV-visible and NIR tissue-simulating phantoms, Opt. Express 14 (2006) 7776, https://doi.org/10.1364/OE.14.007776.
[46] G. Bonnet, O. Krichevsky, A. Libchaber, Kinetics of conformational fluctuations in DNA hairpin-loops, Proc. Natl. Acad. Sci. 95 (1998) 8602–8606, https://doi.org/10.1073/pnas.95.15.8602.
[47] M.N. Berberan Santos, External heavy-atom effect on fluorescence kinetics, PhysChemComm 3 (2000) 18, https://doi.org/10.1039/b002307h.
[48] M.R. Eftink, C.A. Ghiron, Fluorescence quenching studies with proteins, Anal. Biochem. 114 (1981) 199–227, https://doi.org/10.1016/0003-2697(81)90474-7.
[49] M. Sauer, B. Angerer, K.-T. Han, C. Zander, Detection and identification of single dye labeled mononucleotide molecules released from an optical fiber in a microcapillary: first steps towards a new single molecule DNA sequencing technique, Phys. Chem. Chem. Phys. 1 (1999) 2471–2477, https://doi.org/10.1039/A901411J.
[50] J. Widengren, P. Schwille, Characterization of Photoinduced isomerization and Back-isomerization of the cyanine dye Cy5 by fluorescence correlation spectroscopy, J. Phys. Chem. A 104 (2000) 6416–6428, https://doi.org/10.1021/jp000059s.
[51] M.E. Sanborn, B.K. Connolly, K. Gurunathan, M. Levitus, Fluorescence properties and Photophysics of the Sulfoindocyanine Cy3 linked covalently to DNA, J. Phys. Chem. B 111 (2007) 11064–11074, https://doi.org/10.1021/jp072912u.
[52] D. Irving, P. Gong, R. Levicky, DNA surface hybridization: comparison of theory and experiment, J. Phys. Chem. B 114 (2010) 7631–7640, https://doi.org/10.1021/jp100860z.
[53] A. Vainrub, B. Montgomery Pettitt, Surface electrostatic effects in oligonucleotide microarrays: control and optimization of binding thermodynamics, Biopolymers 68 (2003) 265–270, https://doi.org/10.1002/bip.10271.
[54] F. Ricci, A. Vallée-Bélisle, A.J. Simon, A. Porchetta, K.W. Plaxco, Using nature's "tricks" to rationally tune the binding properties of biomolecular receptors, Acc. Chem. Res. 49 (2016) 1884–1892, https://doi.org/10.1021/acs.accounts.6b00276.
[55] B. Esteban Fernández De Ávila, H.M. Watkins, J.M. Pingarrón, K.W. Plaxco, G. Palleschi, F. Ricci, Determinants of the detection limit and specificity of surface-based biosensors, Anal. Chem. 85 (2013) 6593–6597, https://doi.org/10.1021/ac4012123.
[56] S. Gromelski, G. Brezesinski, DNA condensation and interaction with Zwitterionic phospholipids mediated by divalent cations, Langmuir 22 (2006) 6293–6301, https://doi.org/10.1021/la0531796.
[57] M. Mura, B. Humphreys, J. Gilbert, A. Salis, T. Nylander, Cation and buffer specific effects on the DNA-lipid interaction, Colloids Surf. B Biointerfaces 223 (2023) 113187, https://doi.org/10.1016/j.colsurfb.2023.113187.
[58] H. Ravan, S. Kashanian, N. Sanadgol, A. Badoei-Dalfard, Z. Karami, Strategies for optimizing DNA hybridization on surfaces, Anal. Biochem. 444 (2014) 41–46, https://doi.org/10.1016/j.ab.2013.09.032.
[59] M. Sastry, V. Ramakrishnan, M. Pattarkine, K.N. Ganesh, Studies on the formation of DNA–cationic lipid composite films and DNA hybridization in the composites, J. Phys. Chem. B 105 (2001) 4409–4414, https://doi.org/10.1021/jp0034877.
[60] W. Möbius, R.A. Neher, U. Gerland, Kinetic accessibility of buried DNA sites in nucleosomes, Phys. Rev. Lett. 97 (2006) 208102, https://doi.org/10.1103/PhysRevLett.97.208102.
[61] A.M. Poenitzsch Strong, V. Setaluri, V.S. Spiegelman, MicroRNA-340 as a modulator of RAS-RAF-MAPK signaling in melanoma, Arch. Biochem. Biophys. 563 (2014) 118–124, https://doi.org/10.1016/j.abb.2014.07.012.
[62] J. You, M. Kamihira, S. Iijima, Surfactant-mediated gene transfer for animal cells, Cytotechnology 25 (1997) 45–52, https://doi.org/10.1023/A:1007955631313.
[63] M. Dawson, E. Krauland, D. Wirtz, J. Hanes, Transport of polymeric nanoparticle gene carriers in gastric mucus, Biotechnol. Prog. 20 (2004) 851–857, https://doi.org/10.1021/bp0342553.
[64] M.J. Campbell, Lipofection reagents prepared by a simple ethanol injection technique, BioTechniques 18 (1995) 1027–1032.
[65] X. Jiao, R.Y.-H. Wang, Z. Feng, H.J. Alter, J.W.-K. Shih, Modulation of cellular immune response against hepatitis C virus nonstructural protein 3 by cationic liposome encapsulated DNA immunization, Hepatology 37 (2003) 452–460, https://doi.org/10.1053/jhep.2003.50051.
[66] S. Mizuarai, K.-I. Ono, J. You, M. Kamihira, S. Iijima, Protamine-modified DDAB lipid vesicles promote gene transfer in the presence of serum, J. Biochem. 129 (2001) 125–132, https://doi.org/10.1093/oxfordjournals.jbchem.a002822.
[67] S.B. Shelar, A. Dey, S.L. Gawali, S. Dhinakaran, K.C. Barick, M. Basu, S. Uppal, P. A. Hassan, Spontaneous formation of cationic vesicles in aqueous DDAB-lecithin mixtures for efficient plasmid DNA complexation and gene transfection, ACS Appl. Bio Mater. 4 (2021) 6005–6015, https://doi.org/10.1021/acsabm.1c00165.
[68] Y. Jin, S. Wang, L. Tong, L. Du, Rational design of didodecyldimethylammonium bromide-based nanoassemblies for gene delivery, Colloids Surf. B Biointerfaces 126 (2015) 257–264, https://doi.org/10.1016/j.colsurfb.2014.12.032.

[69] M. Ramamoorth, A. Narvekar, Non viral vectors in gene therapy- an overview, J. Clin. Diagn. Res. 9 (2015), https://doi.org/10.7860/JCDR/2015/10443.5394. GE01–GE06.
[70] M. Kucharski, P. Mrowiec, E. Ocłoń, Current standards and pitfalls associated with the transfection of primary fibroblast cells, Biotechnol. Prog. 37 (2021) e3152, https://doi.org/10.1002/btpr.3152.
[71] J. Hahn, S.F.J. Wickham, W.M. Shih, S.D. Perrault, Addressing the instability of DNA nanostructures in tissue culture, ACS Nano 8 (2014) 8765–8775, https://doi.org/10.1021/nn503513p.
[72] Y. Zu, S. Huang, W.-C. Liao, Y. Lu, S. Wang, Gold nanoparticles enhanced electroporation for mammalian cell transfection, J. Biomed. Nanotechnol. 10 (2014) 982–992, https://doi.org/10.1166/jbn.2014.1797.
[73] B. Fejerskov, N.B.S. Jensen, B.M. Teo, B. Städler, A.N. Zelikin, Biocatalytic polymer coatings: on-demand drug synthesis and localized therapeutic effect under dynamic cell culture conditions, Small 10 (2014) 1314–1324, https://doi.org/10.1002/smll.201303101.
[74] C.-Y. Huang, D.-T. Ju, C.-F. Chang, P. Muralidhar Reddy, B.K. Velmurugan, A review on the effects of current chemotherapy drugs and natural agents in treating non–small cell lung cancer, Biomedicine (Taipei) 7 (2026) 23, https://doi.org/10.1051/bmdcn/2017070423.